Formation Mechanisms of the Mesoscale Environment Conducive to a Downslope Windstorm over the Cuyamaca Mountains Associated with Santa Ana Wind during the Cedar Fire (2003)

S. M. SHAJEDUL KARIM,[a,b] YUH-LANG LIN,[a,b] AND MICHAEL L. KAPLAN[c]

[a] *Department of Physics, North Carolina Agricultural and Technical State University, Greensboro, North Carolina*
[b] *Applied Science and Technology, North Carolina Agricultural and Technical State University, Greensboro, North Carolina*
[c] *Department of Applied Aviation Sciences, Embry-Riddle Aeronautical University, Prescott, Arizona*

(Manuscript received 20 March 2022, in final form 10 August 2022)

ABSTRACT: Numerical simulations were conducted to investigate the upstream environment's impacts on the airflow over the lee slope of the Cuyamaca Mountains (CM) near San Diego, California, during the Cedar Fire that occurred from 25 to 29 October 2003. The upstream environment was largely controlled by a southwest–northeast-oriented upper-tropospheric jet streak that rotated around a positively tilted ridge within the polar jet stream. Three sequential dynamical processes were found to be responsible for modifying the mesoscale environment conducive to low-level momentum and dry air that sustained the Cedar Fire. First, the sinking motion associated with the indirect circulation of the jet streak's exit region strengthened the midtropospheric flow over the southern Rockies and the lee slope of the Sawatch and San Juan Ranges, thus modestly affecting the airflow by enhancing the downslope wind over the CM. Second, consistent with the coupling process between the upper-level sinking motion, downward momentum transfer, and developing lower-layer mountain waves, a wave-induced critical level over the mountain produced wave breaking, which was characterized by a strong turbulent mixed region with a wind reversal on top of it. This critical level helped to produce severe downslope winds leading to the third stage: a hydraulic jump that subsequently enhanced the downstream extent of the strong winds conducive to the favorable lower-tropospheric environment for rapid fire spread. Consistent with these findings was the deep-layer resonance between the mountain surface and tropopause, which had a strong impact on strengthening the severe downslope winds over the lee slope of the CM accompanying the elevated strong easterly jet at low levels.

KEYWORDS: Mountain waves; Nonlinear dynamics; Orographic effects; Katabatic winds; Numerical analysis/modeling; Forest fires

1. Introduction

An intense and deadly wildfire, the Cedar Fire, started within the Cleveland National Forest (33.017°N, 116.683°W) near San Diego, California, at 1737 Pacific standard time (PST; UTC − 7) 25 October 2003. The Cedar Fire still remains one of the largest wildfire events in California history (CAL FIRE 2021). The fire was ignited accidentally by a flare from a lost hiker and then subsequently enhanced by Santa Ana winds (Johnson 2004). There were 13 people killed, 105 injured, nearly 273 246 acres (1 acre ≈ 0.4 ha) of forest and urban area burned, and 3021 structures destroyed (CAL FIRE 2003; Johnson 2004).

The surface analysis chart from the National Centers for Environmental Prediction (NCEP) valid at 0000 UTC 25 Oct 2003 is shown in Fig. 1. There is a large, cool, dry ridge of a high pressure over the Great Basin and a low pressure near the Southern California coast. Later, the high pressure over the Great Basin moves equatorward, which results in anticyclonic airflow directed from the northeast toward Southern California's main mountain ranges. This airflow eventually accelerates and develops into a severe downslope wind along the lee slope of the Cuyamaca Mountains (CM), accompanying extreme adiabatic warming and drying Huang et al. (2009, hereinafter HLKC). For detailed observational analysis of the Cedar Fire event, see HLKC, because they examined it comprehensively. Even though the basic dynamics of severe downslope winds have been extensively studied [e.g., Clark and Peltier (1984) and Smith (1985), among others; also see Lin (2007) for a review], the actual mechanisms occurring in specific cases, such as the interactions between upper and lower-level flows over the lee slope and upstream mountain, are complex, nonlinear, and sometimes poorly forecast.

Although the Cedar Fire does not occur over or near the Santa Ana Mountains, its flow characteristics are very similar to those of the well-known Santa Ana windstorm events (Sommers 1978; Small 1995; Glickman 2000; Cao and Fovell 2016; Rolinski et al. 2019). It appears that the Santa Ana winds are responsible for driving the severe downslope winds over the lee slope of the CM, which generate hot, dry, and windy conditions conducive to the Cedar Fire and propagate toward the San Diego coastal area. In this study, we are interested in simulating the complex environment that organized the Cedar Fire to investigate that environment's organizational effects on the downslope winds that occurred over the CM. Note that the CM has a different terrain geometry from that of the Santa Ana Mountains.

The atmospheric conditions upstream of the CM may be influenced by multiple upstream mountain ranges, including 1) the southern portion of the Sawatch Range (SaR), that is, primarily the San Juan Mountains, and to some extent, the Mogollon Rim (MR) in Arizona with an elevation of ~2.5 km and 2) the southern Rockies (SoR) with an elevation of

Corresponding author: Yuh-Lang Lin, ylin@ncat.edu

DOI: 10.1175/JAMC-D-22-0025.1

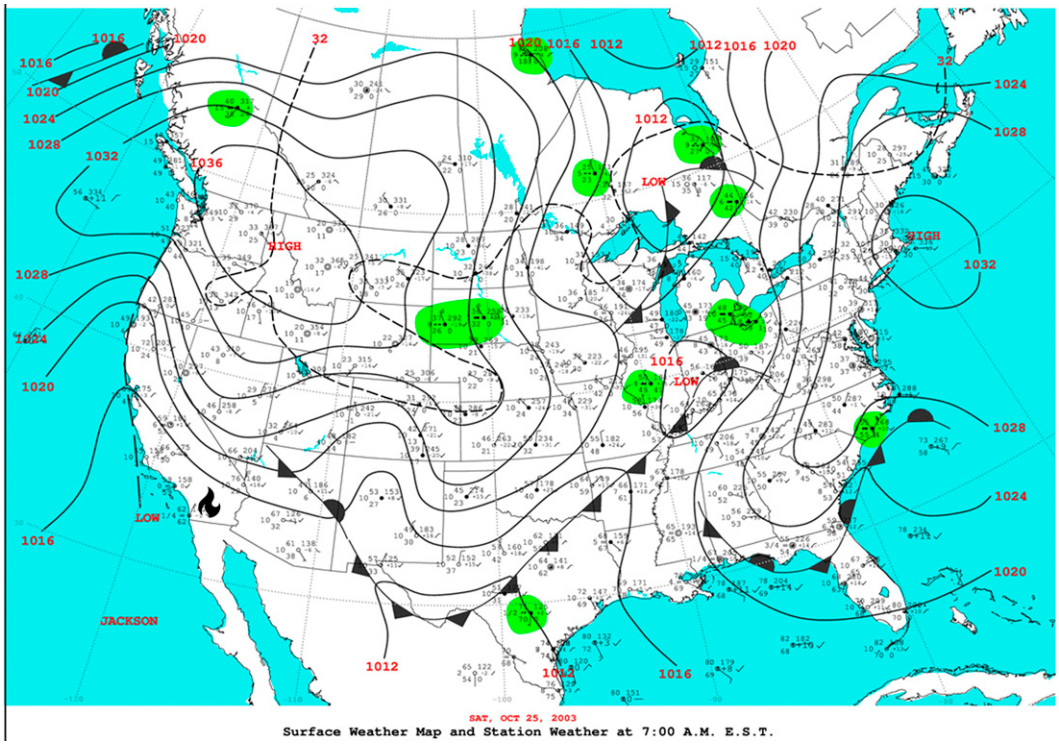

FIG. 1. NCEP Weather Prediction Center observed surface weather analysis map valid at 0000 UTC 25 Oct 2003. The flame symbol denotes the Cedar Fire location in San Diego.

~4 km in southwestern Colorado, that is, primarily the Sangre de Christo Range and the Front Range. In this study, we are interested in studying their potential impacts on the flow characteristics approaching the CM. These flow characteristics include static stability, wind speed, temperature, and relative humidity, which could have been associated with upward-propagating mountain waves, wave breaking, hydraulic jumps (HJ), and severe downslope winds [e.g., Klemp and Lilly (1975); Clark and Peltier (1977); Doyle et al. (2005, 2011); see reviews in Smith (1979) and Lin (2007)].

In particular, in this study, we plan to revisit the coupling of the synoptic-scale and mesoscale forcing leading to the mesoscale environment conducive to the formation of the Cedar Fire in Southern California, as investigated by HLKC. They propose a three-stage conceptual model to illustrate the coupling (Fig. 2). In stages I and II of their conceptual model, the upper-level forcing, which is associated with the sinking motion in the right exit region of an upper-tropospheric jet streak, helps strengthen the downward motion over the southern portion of the SaR. In stage III, the severe downslope wind over the lee slope of the CM strengthens by wave breaking and turbulence. However, in stages II and III, the mesoscale dynamics of severe downslope winds in the lower-tropospheric layer remain poorly understood. For example, one may ask the following questions: (Q1) How does the upper-level forcing couple with the low-level orographically induced severe downslope winds in a series of mountain ranges? (Q2) How do the SaR and, to some extent, MR affect the severe downslope wind over the lee slope of the CM? (Q3) What is the atmospheric state upstream of the CM after passing over the SoR and SaR? (Q4) What are the major mechanisms producing the very strong, dry, and warm downslope winds over the lee slope of the CM? These questions motivate us to investigate the upper- and lower-level coupling mechanism as well as to study the formation mechanisms of the mesoscale environment conducive to the development of the severe downslope wind preceding and during the Cedar Fire.

The dynamics of severe downslope wind over the lee slope of a mountain ridge have been extensively studied in the past (e.g., Long 1953; Klemp and Lilly 1975; Peltier and Clark 1979; Durran and Klemp 1987; Durran 1990; Wang and Lin 1999; Jang and Chun 2010; Lott 2016). Since the early 1980s, two major mechanisms have been proposed to explain the formation of severe downslope winds (e.g., see Lin 2007 for a review): 1) resonant amplification mechanism (Clark and Peltier 1984, hereinafter CP84), and 2) HJ theory (Smith 1985, hereinafter S85). CP84 proposed that a critical level is induced by the mountain waves due to nonlinear wave steepening, overturning, and breaking, which acts to reflect the upward-propagating wave energy back toward the mountain surface, inducing severe downslope winds. When the wave steepens and overturns, a local static instability forms, which helps to produce a well-mixed region. Therefore, a Kelvin–Helmholtz (K-H) instability is triggered after the establishment of a well-mixed region (Scinocca and Peltier 1993;

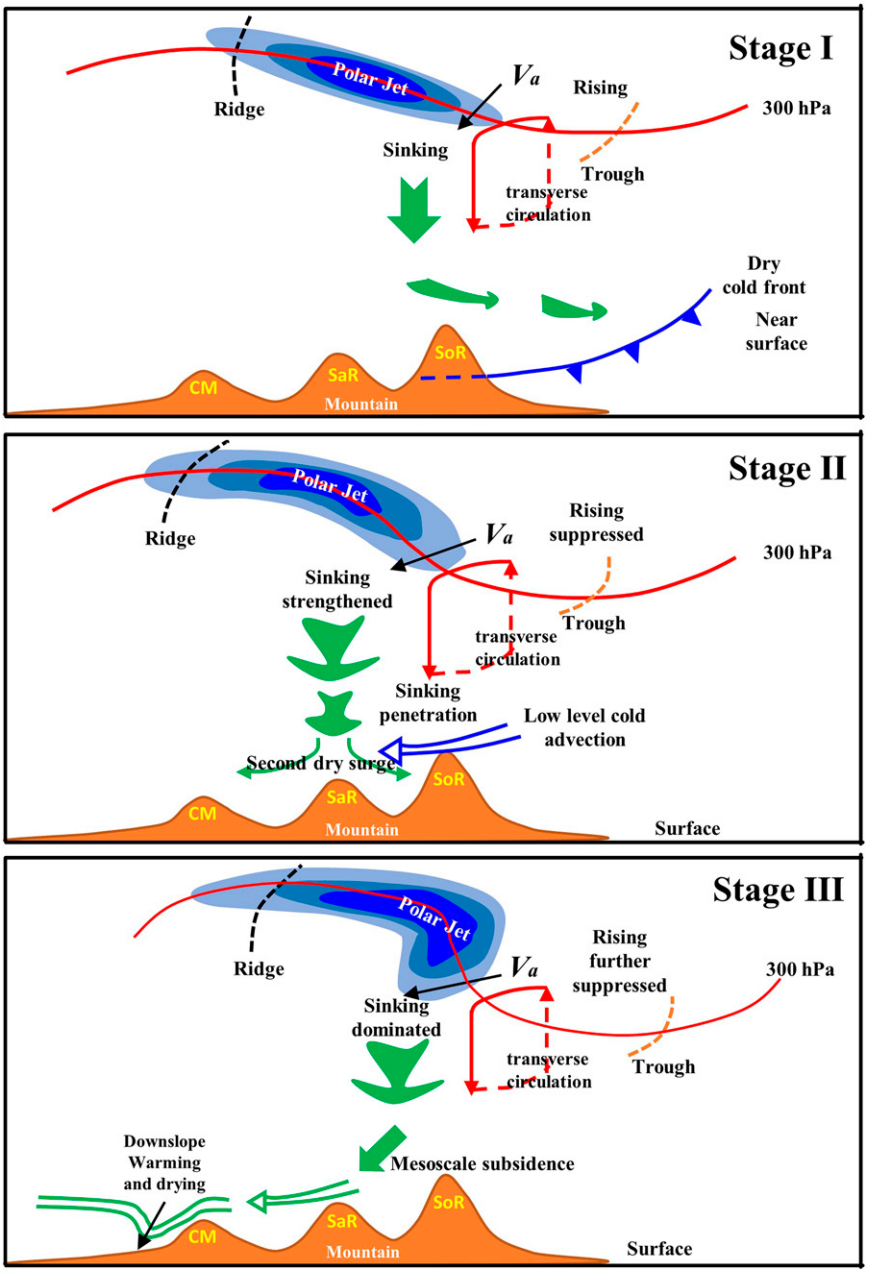

FIG. 2. Three-stage [(top) stage I, (middle) stage II, and (bottom) stage III] conceptual model to illustrate coupling between synoptic and mesoscale environments during the Cedar Fire event, as proposed by HLKC. The mountains from right to left are the Rockies in southwestern Colorado (SoR), the southern portion of the Sawatch Mountain ranges including Mogollon Rim in Arizona (SaR), and the Cuyamaca Mountains (CM) in southwestern California. This figure is adapted from HLKC.

Wang and Lin 1999). According to the other major theory, S85's hydraulic theory, severe downslope winds form by the interaction between a smoothly stratified flow and the deep, well-mixed, turbulent "dead" region aloft above the lee slope in the midtroposphere [see a brief review in Lin (2007), p. 135]. These two theories will be extensively examined in this study.

From the above literature studies, it appears that the synoptic-scale forcing leading to the mesoscale environment conducive to the formation of a downslope windstorm over the lee slope of the CM during the Cedar Fire is not well understood. Therefore, we hypothesize that there exist three consecutive stages experienced by the flow in forming the mesoscale

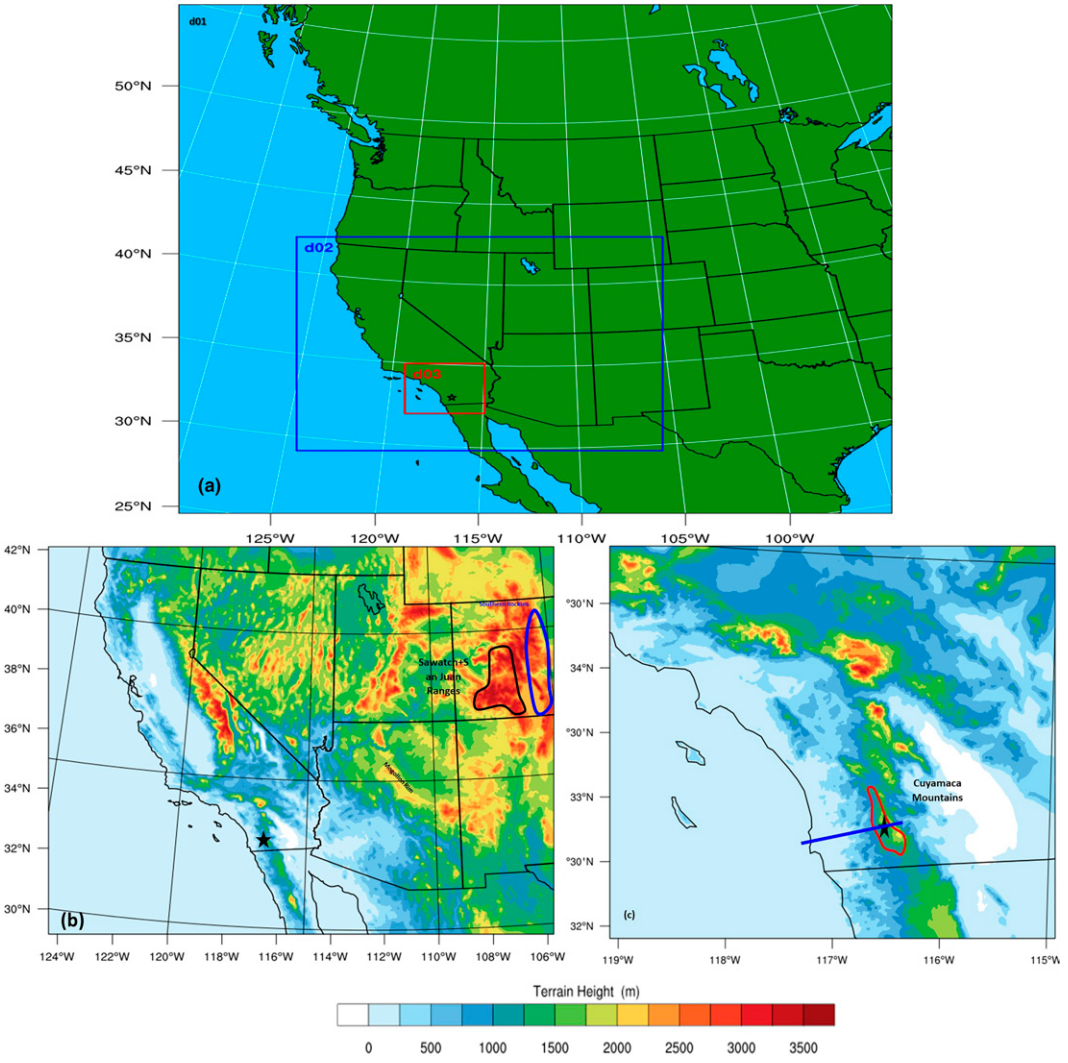

FIG. 3. (a) Domain configuration of the Cedar Fire of d01, d02, and d03 with resolution of 16, 4, and 1 km, respectively. The black star denotes the Cedar Fire location. (b) Terrain geometry of d02, which covers most southwestern states of the United States, including Utah, Arizona, California, Nevada, and part of New Mexico. The terrain height (shaded) is in meters. The thick blue outline indicates the Rockies, and the black outlines indicates the southern portion of the Sawatch and San Juan Ranges. (c) The d03 terrain configuration, which mainly covers southern California, especially San Diego County. The red outline is the location of the Cuyamaca Mountains, where the Cedar Fire formed. The thick blue line is the cross-sectional line oriented from the San Diego coastal region to the Cedar Fire location.

environment over the lee slopes of the CM and Coast Mountain Ranges conducive to the Cedar Fire: 1) the easterly jet in the upper-troposphere is forced downward by the sinking motion associated with a jet streak upstream of the sequence of mountain ranges, 2) a critical layer is induced over the peak of the CM, which results from the resonant amplification mechanism, thus triggering a severe downslope wind over the lee slope of the CM, and then 3) the further enhancement of this severe downslope wind occurs through the HJ mechanism, which propagates downstream to the Coast

TABLE 1. WRF Model domain configuration.

Domain	Dx and Dy (km)	Grid points (x, y, z)	Land use data (arc min)	Time steps (s)
D1	16	225 × 220 × 50	10	60
D2	4	461 × 369 × 50	5	20
D3	1	401 × 345 × 50	2	6

TABLE 2. WRF Model physics parameterization schemes for the simulations.

Physics parameterization	Scheme
Microphysics	Purdue–Lin (Sun and Chen 2002; based on Lin et al. 1983)
PBL	Mellor–Yamada–Janjić scheme (Janjić 1994)
Cumulus (only on D1 and D2)	Kain–Fritsch scheme (Kain 2004)
Surface layer	Monin–Obukhov scheme (Monin and Obukhov 1954)
Land surface	Unified Noah land surface model (Tewari et al. 2004)
Longwave radiation (every 16 min)	Rapid Radiative Transfer Model (RRTM; Mlawer et al. 1997)
Shortwave radiation (every 16 min)	RRTMG (Iacono et al. 2008)

Mountain Range. Note that stages 2 and 3 follow Lin's (2007, p. 137) hypothesis.

Although HLKC have studied stage 1, we will revisit this stage in this study using the Advanced Weather Research and Forecasting (WRF-ARW) model with a higher horizontal resolution, and the second and third stages (2 and 3) will be investigated in this study. In section 2, the model description and numerical experiment design are provided. Verification of the model-simulated synoptic and mesoscale environment for the Cedar Fire will be presented in section 3. The mechanisms responsible for producing the severe downslope winds are investigated in depth in section 4. Conclusions and discussion are given in section 5.

2. Numerical experiment

a. Numerical experiment overview

The abovementioned objectives will be accomplished by conducting both real data and idealized numerical simulations. We will first conduct real data simulations. By doing so, we will determine how the larger-scale environment is established, which favors a mesoscale environment that is conducive to the occurrence of the downslope winds that enhanced the Cedar Fire. The coarse-resolution simulated results will be validated by synoptic observations, including the fifth major global reanalysis produced by ECMWF reanalysis data (ERA5; ECMWF 2019), sounding profiles, and so on. Terrain sensitivity experiments will be performed by removing specific mountain ranges, such as the SaR, and the SoR. This will be done to investigate their roles in affecting the atmospheric conditions after the flow passing over them is perturbed and subsequently influences the airflow passing over the CM. Then, we will analyze the results from a finer-resolution simulation to identify the dynamic processes leading to the downslope winds over the lee slope of the CM. We will also conduct several idealized simulations using soundings extracted from the coarse-resolution simulation upstream of the mountains.

b. Numerical model and experimental design

1) REAL-CASE WRF SIMULATIONS

The WRF-ARW Model, version 4.0 (Skamarock et al. 2019), is employed for the numerical simulations of the Cedar Fire in this study. The simulations use one-way triple-nested domains: d01 (D1), d02 (D2), and d03 (D3) with a horizontal grid spacing of 16, 4, and 1 km, respectively. D1 captures the core of the synoptic pattern controlling the environment surrounding the Cedar Fire event. D2 covers Utah, Arizona, California, Nevada, and part of New Mexico, and D3 covers Southern California, especially San Diego County. Figure 3 shows the domain configuration of D1, D2, and D3. The southern portion of the SaR, and the SoR are depicted in Fig. 3b (see thick black outline shape for SaR and blue outline shape for SoR). The CM is depicted in Fig. 3c (see thick red outline shape). The vertical grid configuration contains 50 levels with a domain-top height of 10 hPa, which was found to most accurately simulate the vertical motions in the study of Karim and Lin (2021). The domain configuration of the WRF Model is summarized in Table 1. The WRF Model

TABLE 3. Summary of real data numerical experiments.

Case	Key features	Remarks
CNTL	Real control case; three nested domains with Δx = 16 km (D1), 4 km (D2), and 1 km (D3); initialized at 0000 UTC 25 Oct and ending at 0000 UTC 27 Oct 2003; domain top = 10 hPa; vertical grid levels = 50	Captures the prevailing condition for the formation of the Cedar Fire and produces severe downslope wind over the lee slope of the CM
NoSa	Same as CNTL case except 1) it is run on only the 16-km coarse domain and 2) Sawatch Range, including Mogollon Rim in Arizona, is removed	Reduces the strength of the downslope wind over the CM
NoRo	Same as CNTL case except 1) it is run on only the 16-km coarse domain and 2) the southern Rockies in Colorado are removed	Reduces the strength of the downslope wind
NoSR	Same as CNTL case except 1) it is run on only the 16-km coarse domain and 2) the southern Rockies and Sawatch Ranges are both removed	The downslope wind over the CM is stronger than in the CNTL case

TABLE 4. Summary of idealized numerical experiments.

Case	Key features	Remarks
ICTL	Idealized control case; 2D bell-shaped mountain with h_m = 1.5 km and width a = 10 km; model top is 20 km; run for 12 h; uniform basic wind $U = -7.5$ m s^{-1} with structured Brunt–Väisälä frequency N	Represents the resonance between the mountain surface and the tropopause, which is produced by the orographically induced gravity waves and the sudden increase of N at the tropopause
IJET	Same as ICTL except with a wind jet added around the tropopause in the idealized sounding	No resonance in the midtroposphere
INN	Same as ICTL except with no variation of N in the idealized sounding, representing a case with no stratosphere	No longer see strong reflection in comparison with that in the ICTL case

physical parameterization schemes chosen for the simulations are described in Table 2.

We use NCEP's GFS final (FNL) 1° × 1° reanalysis data (NCEP 2000) to initialize the model in this study. The domain D1 simulation is initialized by GFS data at 0000 UTC 25 October and integrated for 48 h, the domain D2 simulation is initialized by the output of D1 at 1200 UTC 25 October and integrated for 36 h, and the domain D3 simulation is initialized at 0000 UTC 26 October and integrated to 0000 UTC 27 October 2003. The 16-km simulation serves as the initial and boundary conditions for the 4-km case, and the 4-km simulation case serves as the initial and boundary conditions for the 1-km case. We refer to this simulation as the control (CNTL) case for the rest of this study. In addition to the CNTL case simulation, three terrain sensitivity experiments are performed by removing a specific mountain range. First, we remove the SaR (NoSa); second, we remove the SoR (NoRo); and third, we remove both the SaR and SoR (NoSR). These sensitivity experiments are summarized in Table 3. Note that we use only a 16-km (D1) coarse domain to conduct those three terrain sensitivity experiments.

2) IDEALIZED WRF SIMULATIONS

To understand the basic dynamics of severe downslope winds from the terrain sensitivity experiments, we conduct idealized WRF simulations using upstream sounding. In this study, the upstream sounding has been extracted from real data coarse-resolution (NoSR) simulation to initialize the WRF idealized sensitivity experiments. The simulations are integrated in 2D mode with 1-km horizontal grid spacing and grid points of 402 in the x direction. There are 126 grid levels (e.g., Doyle et al. 2011) in the z direction stretched from the surface to the model top (20 km). The model has a sponge layer set between 15 km and the domain top to absorb wave energy generated in the physical domain, giving the model a sponge-layer depth of 5 km. A free-slip boundary condition is applied at the bottom boundary. Rotational effects are ignored by setting the Coriolis parameter to zero. A 2D bell-shaped mountain represents the idealized terrain, described by the equation

$$h(x) = \frac{h_m}{(x/a)^2 + 1},$$

where h_m is the mountain height, and a is the half-width. We use the fixed mountain height of 1.5 km and half-width of 10 km for all simulations to make it consistent with the actual CM height.

Three idealized simulations were performed to study the specific effect of different parameters on producing severe downslope winds over the lee slope of the CM during the Cedar Fire. These cases include idealized control (ICTL) (with uniform basic wind and structured Brunt–Väisälä frequency N), IJET (with strong upper-level jet), and INN (with constant $N = 0.01$ s^{-1}). A detailed explanation of these three cases is given in section 4c and summarized in Table 4. All simulations are integrated for 12 h, and the simulated fields are archived every hour.

3. Model verification of the synoptic and mesoscale environments for the Cedar Fire environment

Although well-documented verification of simulated Cedar Fire's synoptic-scale features with observations are presented in HLKC, we revisit some parts of the verification in this study as we use a more advanced mesoscale WRF Model with higher horizontal resolution. Figure 4 shows the 16-km simulated mean sea level pressure, surface wind barbs (Fig. 4b) and the sea level pressure from ERA5 reanalysis (interpolated to 16-km resolution from 0.25° × 0.25° horizontal resolution) (Fig. 4a), valid at 0900 UTC 25 October 2003. A significant region of high pressure began to build equatorward from the Pacific Northwest to the Great Basin on 25 October. In response to the building high, an east–west offshore pressure gradient became established over Southern California. In the simulation, a significant high pressure center of ~1036 hPa is observed over the Great Basin, which is almost identical to the ERA5 (~1037 hPa). At the same time, a low pressure area near the northern coast of Baja California and an inverted trough extending up the California coast can be seen in both the 16-km simulated (lowest = 1011 hPa) and ERA5 (lowest = 1012 hPa) data.

Figure 5 shows the 300-hPa isotachs, geopotential height, and winds in the 16-km simulation (Figs. 5a,b) and ERA5 reanalysis (Figs. 5c,d) valid at 0300 UTC 25 and 1200 UTC 26 October. The WRF 16-km simulation replicates the ERA5 reanalysis large-scale features, although the strongest core of momentum at 1200 UTC is underdone across the key region

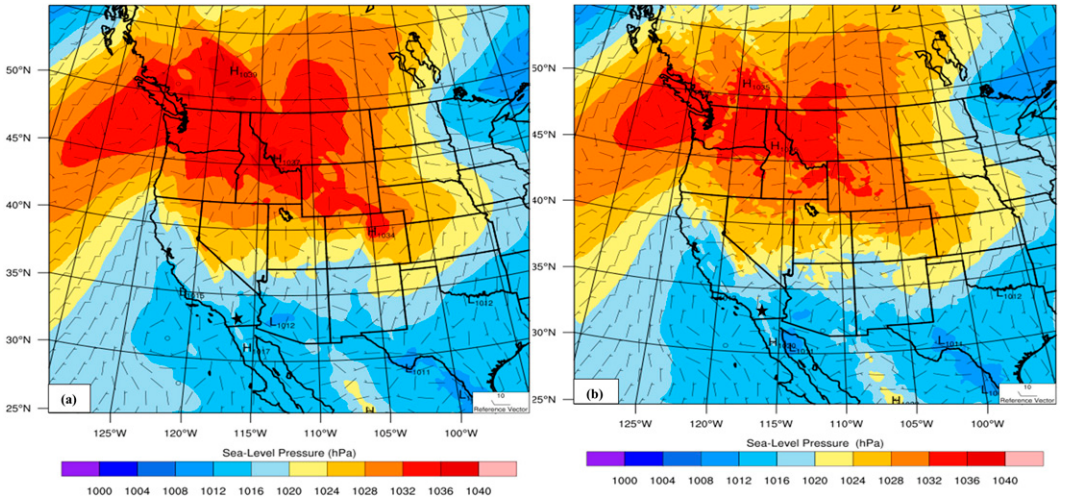

FIG. 4. (a) The sea level pressure (shaded; hPa) and winds of the ERA5 reanalysis (interpolated to 16-km resolution from 0.25° × 0.25° horizontal resolution), and (b) the 16-km simulated sea level pressure and wind barbs (m s^{-1}) valid at 0900 UTC 25 Oct 2003. The black star denotes the Cedar Fire location.

from Colorado to New Mexico in the simulation by ~10 m s^{-1}. A simulated jet streak (>50 m s^{-1}) at 300 hPa is present over the northwestern part of the United States and southwestern Canada at 0300 UTC 25 October (Figs. 5a,c), which indicates the formation of the synoptic environment favorable for offshore flow. A positive (anticyclonically tilted) upper-level trough is observed over the Great Basin at 0300 UTC 25 October (Fig. 5a). This upper-level trough intensifies and turns the synoptic-scale wind equatorward first down the eastern Sierra Nevada and subsequently across Arizona into Southern

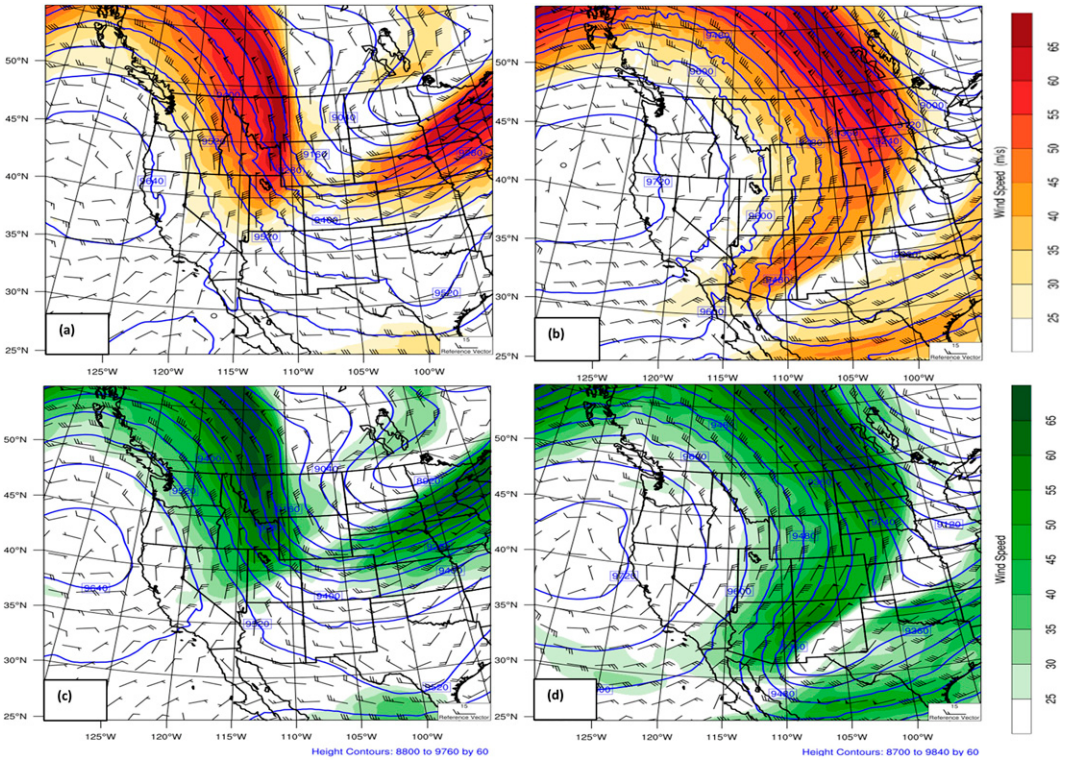

FIG. 5. Analysis of 300-hPa isotachs (shaded; m s^{-1}), geopotential height (blue contours; m), and wind barbs (m s^{-1}) from the (a),(b) 16-km WRF simulation and (c),(d) ERA5 reanalysis (interpolated to 16-km resolution from 0.25° × 0.25° horizontal resolution) valid at (left) 0300 UTC 25 and (right) 1200 UTC 26 Oct 2003.

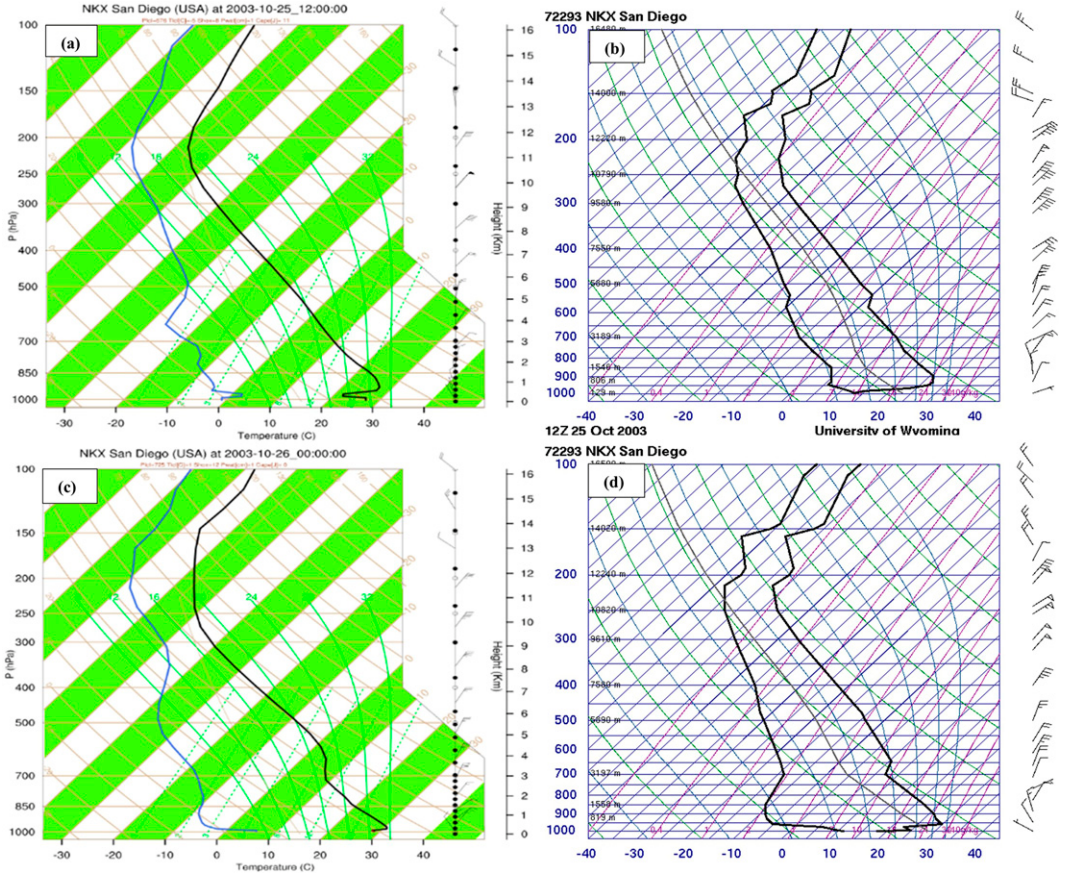

FIG. 6. Thermodynamic diagrams extracted for the NKX San Diego station from the (a),(c) 4-km WRF simulation and (b),(d) UWyo observationaldata valid at (top) 1200 UTC 25 and (bottom) 0000 UTC 26 Oct 2003.

California and became more anticyclonically curved in time (Figs. 5b,d).

A direct comparison of fine-resolution (4 km) WRF simulated sounding data with the University of Wyoming (UWyo) sounding data is examined below to determine any model biases or errors near the fire location. The thermodynamic diagram for the NKX San Diego station simulated and observed are in Fig. 6. Two different atmospheric layers exist near the fire location in both the observed and simulated soundings at 0000 UTC 26 October. In the lower layer (below 950 hPa), the air was cooler and moister, which likely originated from the northwest (Pacific Ocean) based on the wind direction. The temperature increased with height, reached its maximum at about 950 hPa, and then decreased adiabatically above. The air is much dryer in the upper layer and reverses its direction, originating from the northeast, associated with the upper-level, inland synoptic high pressure system. The reversal of wind direction at ~850 hPa is the primary signal of a critical level, which is likely wave induced. The thermodynamic diagrams analyzed from the 4-km WRF simulated flow fields accurately capture observed temperature profiles, lower dry layer, wind speed and its direction and wind reversal in the low levels. However, it is seen that the simulated temperature inversion layer has been somewhat smoothed in comparison with the observations.

Overall, the simulated synoptic-scale and meso-α-scale weather pattern analysis looks consistent with observations. In a nutshell, with the presence of strong high pressure over the Great basin area and low pressure near the coast of southern California, the upper-level jet streak was observed over the northwestern United States. This upper-level jet transported dry air toward the Southern California coast, producing mountain-induced severe downslope winds in the Cedar Fire location. The detailed formation mechanisms of downscale winds will be diagnosed in the next section.

4. Mechanisms of severe downslope wind formation during the Cedar Fire

After conducting numerical simulations using the WRF-ARW model, we find that the following three mechanisms occurred in sequence to produce severe downslope winds over the lee slope of the CM, creating a favorable environment for the Cedar Fire (2003): (i) upper-level jet forcing mechanism (HLKC), (ii) resonant amplification mechanism (CP84), and (iii) HJ mechanism (S85). These three mechanisms have been briefly reviewed in section 1.

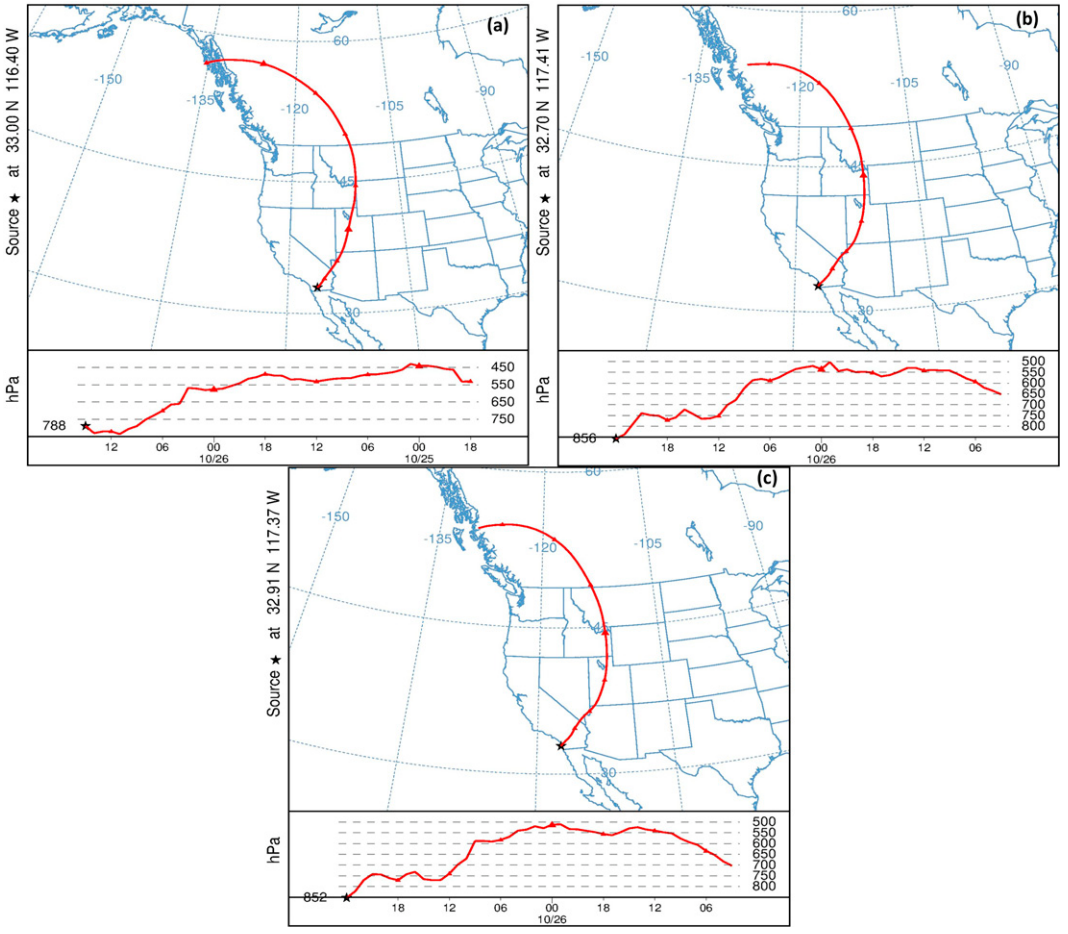

FIG. 7. Backward-trajectory analysis of three air parcels released at 850 hPa from the (a) Cedar Fire location, (b) location at 32.7°N, 117.41°W, and (c) location at 32.091°N, 117.37°W. The black star denotes the released location of the air parcels. The model was initialized with the 16-km WRF-simulated output starting from 0000 UTC 27 Oct and ending at 0000 UTC 25 Oct 2003.

a. Impacts of the upper-level jet streak, the SaR, and the SoR on the formation of severe downslope wind over the lee slope of the CM

In this section, we will try to answer questions Q1–Q3 to investigate the impact of sinking motion associated with the upper-level jet streak exit region on the low-level flow over the sequence of mountain ranges, for example, the SoR, SaR, and CM.

The sinking motion associated with the meso-α/meso-β upper-level jet streak can be traced by backward-trajectory analysis. The backward-trajectory analysis shows the source of the air parcels arriving at the fire location. The NOAA Hybrid Single-Particle Lagrangian Integrated Trajectory model (HYSPLIT; Stein et al. 2015) is used to generate the backward trajectory, which is initialized with the WRF CNTL-simulated data. We have chosen only three air parcels to ensure that our WRF-simulated sinking motion associated with the upper-level jet follows the anticyclonic jet curvature and reaches the fire location. For more detailed backward-trajectory analysis, readers are referred to HLKC because they considered 24 air parcels. Three air parcels are released at 850 hPa from three different locations, one at the Cedar Fire location (33.0°N, 116.40°W) and the other two in proximity to the fire location at 32.7°N, 117.41°W and 32.091°N, 117.37°W. Figure 7 shows the backward trajectories of these three air parcels starting at 0000 UTC 27 October and ending at 0000 UTC 25 October. All three air parcels originated from southwestern coastal British Columbia and descended following an anticyclonically curved trajectory to reach the fire location. The air parcel released at the Cedar Fire location (Fig. 7a) descends dramatically after 1800 UTC 25 October 2003, as the upper-level jet starts to tilt anticyclonically. Since the air parcels descended and converged from the meso-α scale to the meso-β scale, the air parcels warmed and dried through the adiabatic warming process (see the backward trajectories in Fig. 14 of HLKC). The upper-level air parcels interact with the air near the high terrain in the southwestern United States when they descend to the top of the PBL. This interaction will be investigated through cross-sectional analyses.

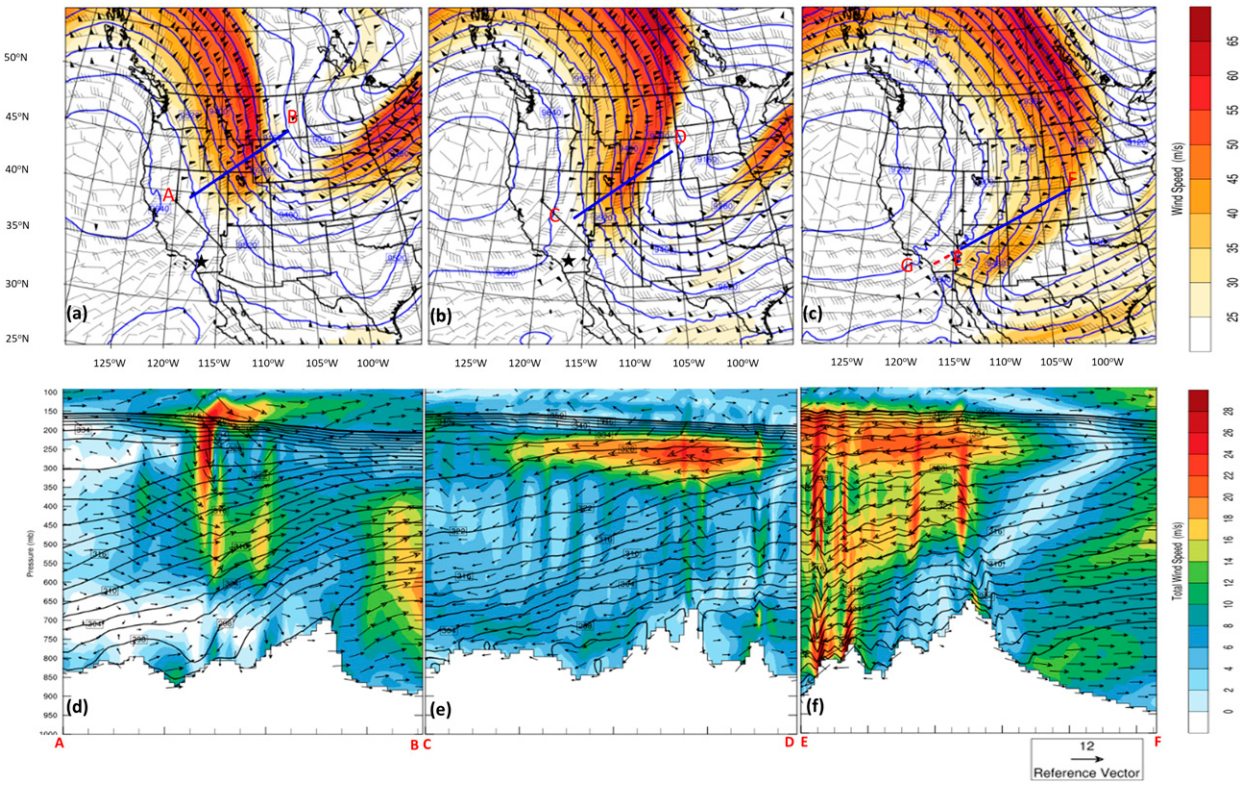

FIG. 8. The 16-km simulated 300-hPa wind barbs, wind speed (shaded; m s^{-1}), and geopotential height fields at (a) 0300 UTC 25, (b) 1800 UTC 25, and (c) 1200 UTC 26 Oct. Four different cross sections—AB, CD, EF, and GF—are also depicted in (a)–(c). The latitudes and longitudes for the end points of AB, CD, EF, and GF are 39.1°N, 116.93°W for A; 45°N, 107.8°W for B; 36.5°N, 117°W for C; 42.5°N, 108°W for D; 34°N, 114.5°W for E; 40°N, 102°W for F; and 32.7°N, 118.6°W for G. Also shown is the vertical cross-sectional analysis of total wind speed $(u^2 + w^2)^{1/2}$ (shaded; m s^{-1}), potential temperature (contours; K), and wind vectors (u, w; arrows) along (d) AB, (e) CD, and (f) EF for the corresponding times.

We choose four different cross sections from the CNTL case orthogonal to the upper-level jet streak in the exit region, which are following the movement of the jet streak, as depicted by AB, CD, EF, and GF in Figs. 8a, 8b, and 8c, respectively. These cross sections lie over the northern, central, and southern Great Basin. All wind component vector (u, w), total wind speed $(u^2 + w^2)^{1/2}$, and potential temperature fields along the AB, CD, and EF vertical cross sections at 0300 UTC 25, 1800 UTC 25, and 1200 UTC 26 October are analyzed in Figs. 8d–f.

At 0300 UTC 25 October (Figs. 8a,d), the nearly straight jet streak at 300 hPa has weak sinking motion in the right exit region consistent with a four-cell pattern (e.g., see Fig. 10.20 of Lin 2007). Therefore, a transverse ageostrophic thermally indirect circulation is observed in the jet exit region. As the upper-level jet streak advances equatorward (Figs. 8b,e), the circulation associated with it starts to tilt anticyclonically and increases the nonlinearity. Once the straight jet streak becomes curved, its four-cell pattern starts to shift to a two-cell pattern, as can be inferred from the shift in the descent toward the along, as opposed to cross-stream exit region location near 400 hPa in Fig. 8e (e.g., Clark et al. 2009). Therefore, the downward motion consistent with the back trajectories starts to concentrate within the jet exit region and the flow pattern splits into the northeasterly and northwesterly flow near the border region of Nevada, Arizona, Colorado, and Utah. After 18 more hours of propagation (Figs. 8c,f), the upper-level jet streak tilted more anticyclonically equatorward over the peak of the SaR in southwestern Colorado. The strengthening downward motion caused by the curved and convergent flow over and southwest of Colorado forced northeasterly flow to penetrate to 750 hPa (Fig. 8f). Since the upper-level air descends as it approaches the lee slopes, it tends to help strengthen the severe downslope wind over the lee slopes of the SaR.

Cross section EF is extended farther to the west to San Diego (red dotted line GF in Fig. 8c). The approximate maximum heights of the three major mountain ranges along this cross section from west to east are: $h_m \approx 1.9$ km over the CM (left small mountain), ~2.5 km over the southern portion of the SaR (middle mountain), and ~4 km over the SoR (right big mountain). This new cross section allows us to examine whether there is a coupling between upper-level jet-induced downward motion and lower-level mountain waves in producing severe downslope winds near the Cedar Fire location. The 3D wave structure of the total wind speed $(u^2 + w^2)^{1/2}$,

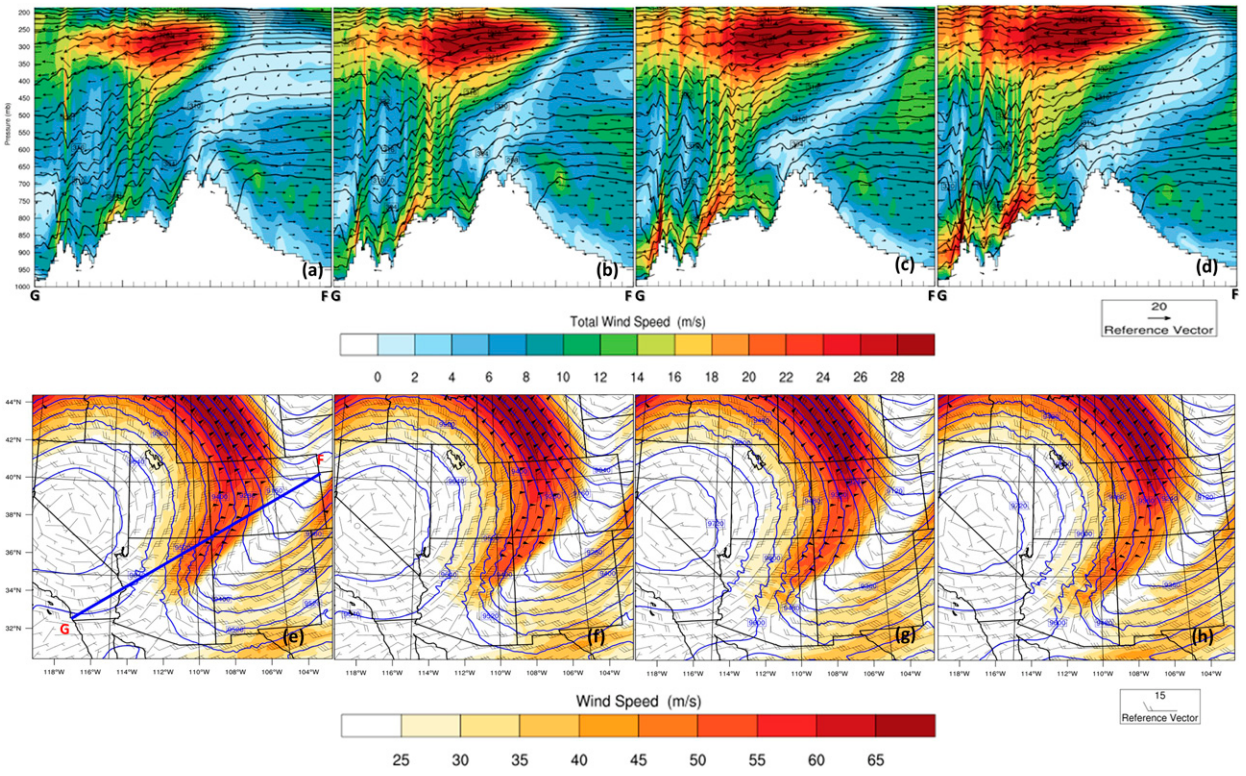

FIG. 9. The 3D structure of the total wind speed $(u^2 + w^2)^{1/2}$ (shaded; m s^{-1}), potential temperature (contours; K), wind vectors (u, w; arrows) fields on cross section GF of the CNTL case extending from northeast to southwest valid at (a) 0200, (b) 0400, (c) 0600, and (d) 0800 UTC 26 Oct 2003. Toward the southwest is the Cuyamaca Mountains, the southern portion of the Sawatch Range is in the center of each figure, and the Rockies are toward the northeast. (e)–(h) The corresponding 2D horizontal structure of the jet at 300-hPa level zoomed over a small cross-sectional area of the CNTL case, showing . The wind isotachs $(u^2 + v^2)^{1/2}$ (shading; m s^{-1}), wind barbs (u, v) (kt; 1 kt ≈ 0.51 m s^{-1}), and geopotential height fields (blue contours; dam). In (e), the thick blue line depicts the cross section GF.

potential temperature, and wind vectors (u, w) along the GF cross section valid from 0200 to 1600 UTC 26 October 2003 is shown in Figs. 9a–d and 10a–d. To relate the interaction of downward motion in the jet exit region to the lower-level mountain waves, the corresponding 2D horizontal structure of the jet isotachs at the 300-hPa level zoomed in over a small cross-sectional (GF) area of the CNTL case are shown in Figs. 9e–h and 10e–h, respectively.

At 0200 UTC 26 October (Figs. 9a,e), there exist no apparent interactions between the upper-level sinking motion and the mountain waves produced by the orography. Two hours later, at 0400 UTC 26 October (Figs. 9b,f), the downward motion starts to increase in response to the anticyclonic curvature of the upper-level jet streak. At 0600 UTC 26 October (Figs. 9c,g), the mountain wave activity is over the lee slope of the SaR as well as MR as the sinking motion penetrates to the top of the PBL (see backward trajectory in Fig. 7). These mountain waves extend to the fire location over the CM. Since the sinking motion dominates the jet exit region for the next couple of hours (see Figs. 9h and 10e–h), the strength of the mountain waves induced by the CM increases (see Figs. 9d and 10a–d) and produces its maximum severe downslope wind of ~32 m s^{-1}. Therefore, the upper-level sinking motion is coupled to the mountain waves associated with the southern portion of the SaR, that is, the San Juan Mountains and the MR, enhancing the severe downslope winds over the lee slope, which continues through the afternoon of 27 October. However, the impacts of the upper-level sinking motion and its interactions with the orographic forcing on the formation of the severe downslope winds over these ensembles of mountains in the SoR are still not clear. From the flow of the CNTL case (Figs. 9 and 10), it seems that the SaR and neighboring ranges play an essential role in producing severe downslope wind over the lee slope of the CM. The combined effects of the sinking motion associated with the upper-level jet streak and these southern Rockies will be further investigated in the next section.

To investigate the orographic impacts on the sinking motion associated with the jet streak in concert with the SoR and SaR producing the severe downslope wind over the CM, we run three terrain sensitivity experiments by removing 1) the southern portion of the SaR (NoSa), 2) SoR (NoRo), and 3) both SaR and SoR (NoSR) from the CNTL case (see Table 3 for a summary). Figure 11 shows the vertical cross section of the total wind speed $(u^2 + w^2)^{1/2}$, potential temperature, and wind vector (u, w) fields for case NoSa

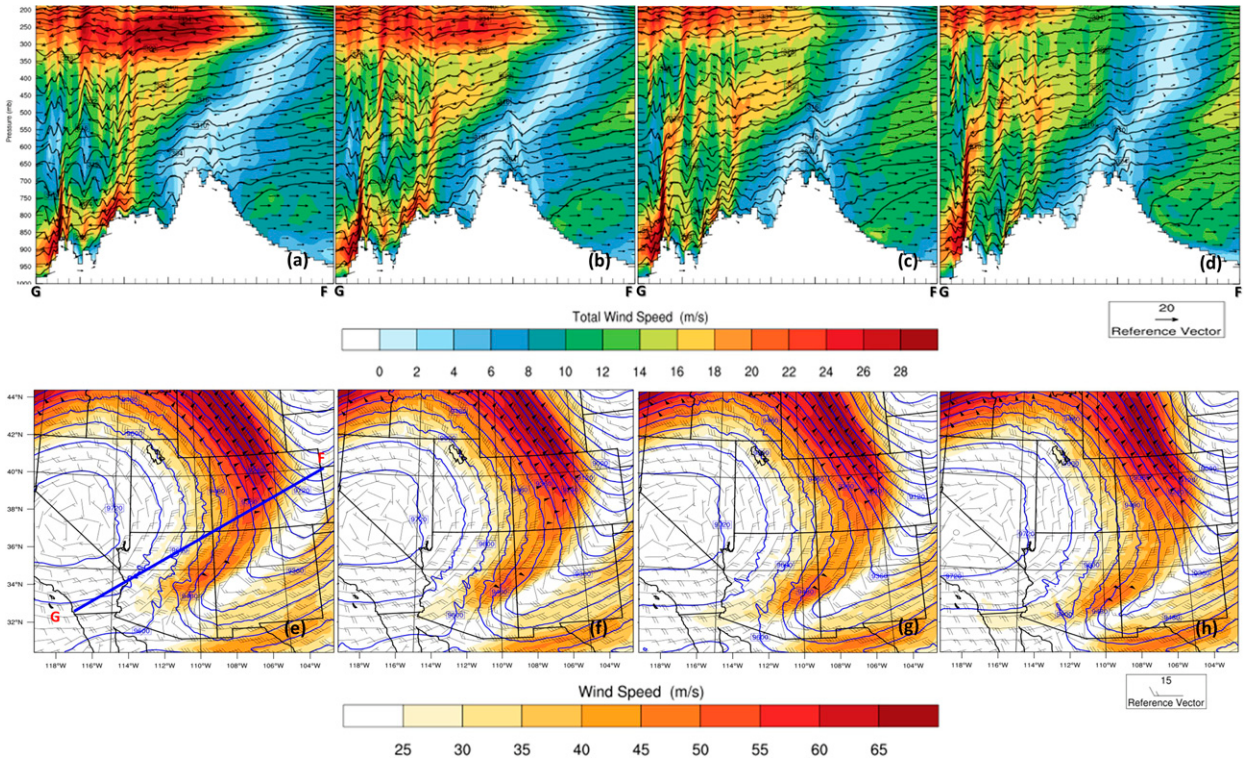

FIG. 10. As in Fig. 9, but valid at (a),(e) 1000 UTC; (b),(f) 1200 UTC; (c),(g) 1400 UTC; and (d),(h) 1600 UTC 26 Oct 2003.

from 0200 to1600 UTC 26 October for every 2 h. When the SaR and neighboring mountains are not present, the air descends down to very low levels near the flat surface on the western edge of the SoR, following a deep pool of low-level, strong easterly flow in between the SoR and CM (Figs. 11a–c). This pool of strong easterly airflow is a transient phenomenon due to the descending motion and weakens quickly from 0800 to 1200 UTC 26 October (Figs. 11d–f). Consequently, no mountain waves exist in the layer above 1.5 km (Figs. 11e–h). However, this downslope and westward-moving air helps to enhance the strong downslope wind over the lee slope of the CM, which reaches a maximum of ~20 m s^{-1}, which is not as strong as the CNTL case (~32 m s^{-1}). Thus, case NoSa indicates that the presence of the SaR and neighboring mountains do not enhance the strong downslope wind over the CM. The impacts of the SoR (high and large mountain range), including the Sangre de Christo, Front Range in Colorado, have been investigated by conducting a terrain sensitivity experiment with its terrain removed from the 16-km domain (case NoRo). The analysis of this case (not shown) shows a weak coupling between the upper-level downward motion and lower-level flow, similar to the NoSa case. It induces a weaker downslope wind (maximum wind ~22 m s^{-1}) over the lee slope of the CM relative to the CNTL case.

The combined impact of SaR and SoR on the severe downslope wind over the CM is further investigated by removing both mountain ranges (NoSR). Figure 12 shows that there is no apparent sinking motion associated with the upstream flow in the region of the removed SaR and SoR. Surprisingly, this case produces stronger downslope winds over the lee slope of the CM at earlier times (Figs. 12a–c) relative to no strong downslope wind at the same times in the CNTL case (see Figs. 9a–c). Since there exists no apparent descending motion upstream of the CM in this case, we may conclude that the upstream descending motion is not a necessary condition for the formation of severe downslope winds over the CM; instead, it appears due to the resonance between the upper stratospheric layer and the flow near the CM surface. To understand the dynamics of severe downslope wind in the NoSR case without having upper-level descending motion, we conduct idealized numerical simulations by extracting an upstream sounding from the NoSR case. The results from those idealized experiments will be investigated in section 4c.

From cases CNTL, NoSa, NoRo (not shown), and NoSR, we may conclude that the SaR and the SoR do not play significant roles in producing the severe downslope wind over the CM where the Cedar Fire occurs. In other words, the southern portion of the SaR and the SoR have modified the upstream condition to weaken the severe downslope wind over the lee slope of the CM. The sinking motion associated with the upper-level jet streak appears to be able to enhance the downslope winds over the lee slope of the CM; however, it is not a necessary condition for producing them. Thus, we have verified the hypothesis or stage 1, as

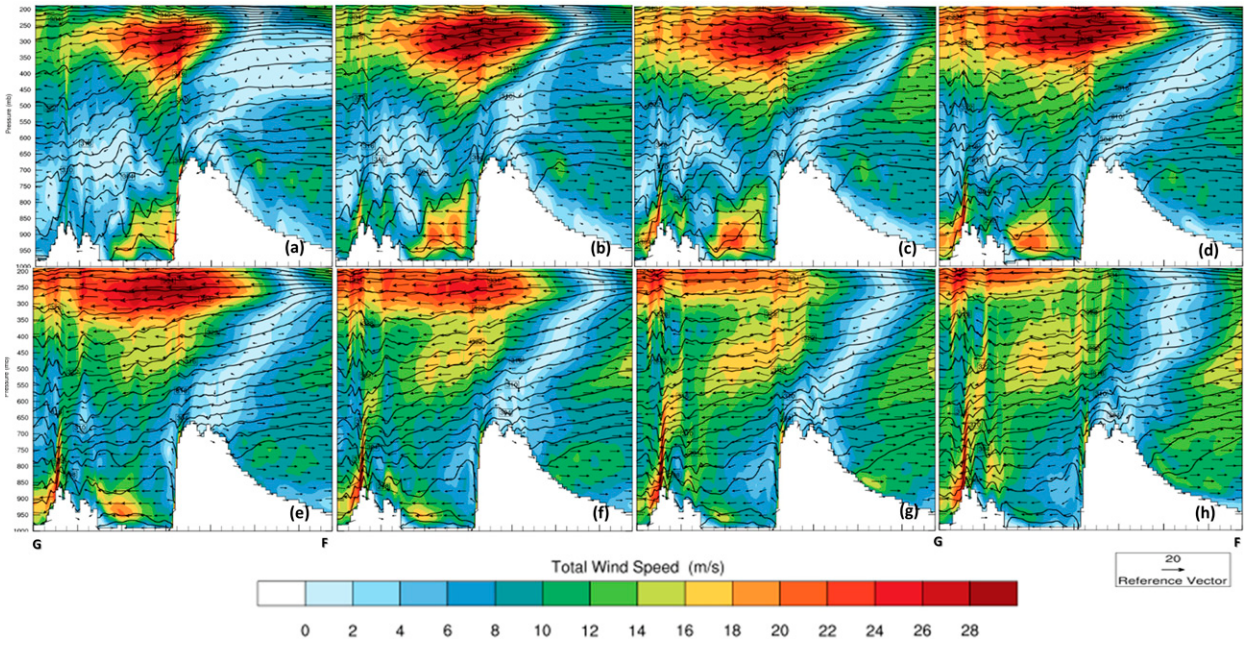

FIG. 11. Total wind speed of $(u^2 + w^2)^{1/2}$ (shaded; m s^{-1}), potential temperature (contours; K), and wind vector (u, w; arrows) fields on cross section GF of the NoSa case: (a) 0200 UTC, (b) 0400 UTC, (c) 0600 UTC, (d) 0800 UTC, (e) 1000 UTC, (f) 1200 UTC, (g) 1400 UTC, and (h) 1600 UTC 26 Oct 2003.

proposed in the introduction section: the easterly wind in the upper troposphere is forced downward by the sinking motion associated with a jet streak upstream of the three mountain ranges.

b. *Formation of the severe downslope wind over the lee slope of CM*

In this section, we would like to verify stages 2 and 3 of the hypothesis proposed in the introduction section: 2) a critical

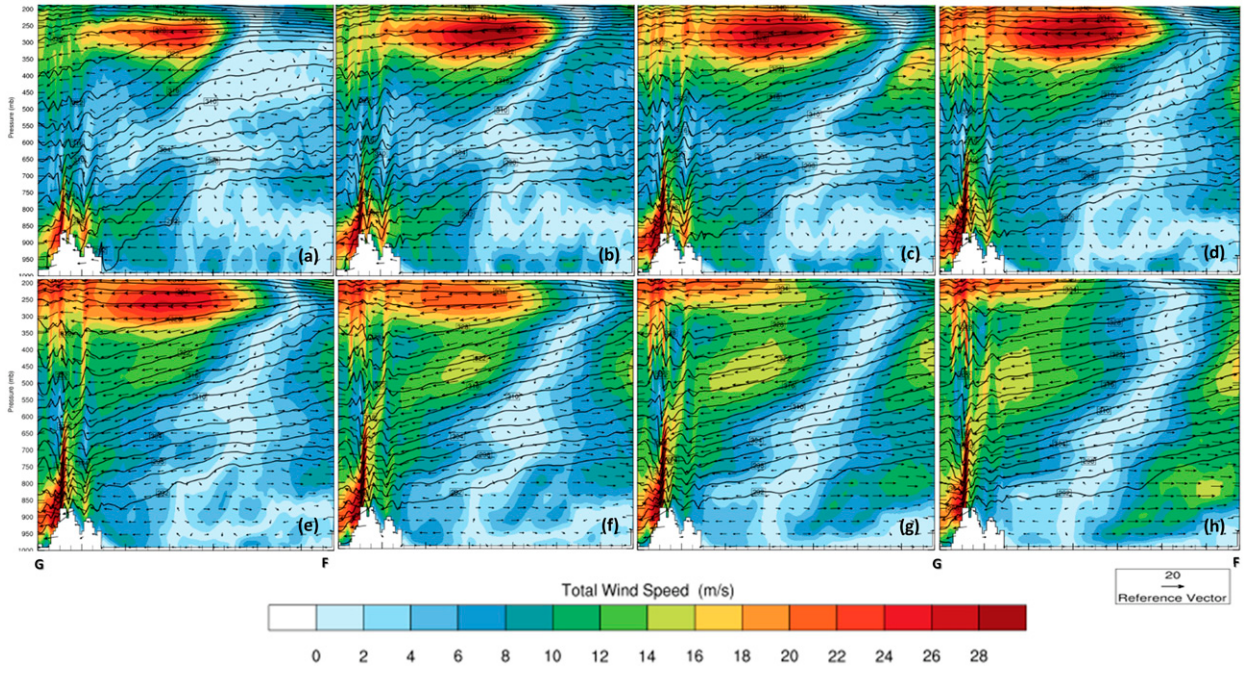

FIG. 12. As in Fig. 11, but for the NoSR case.

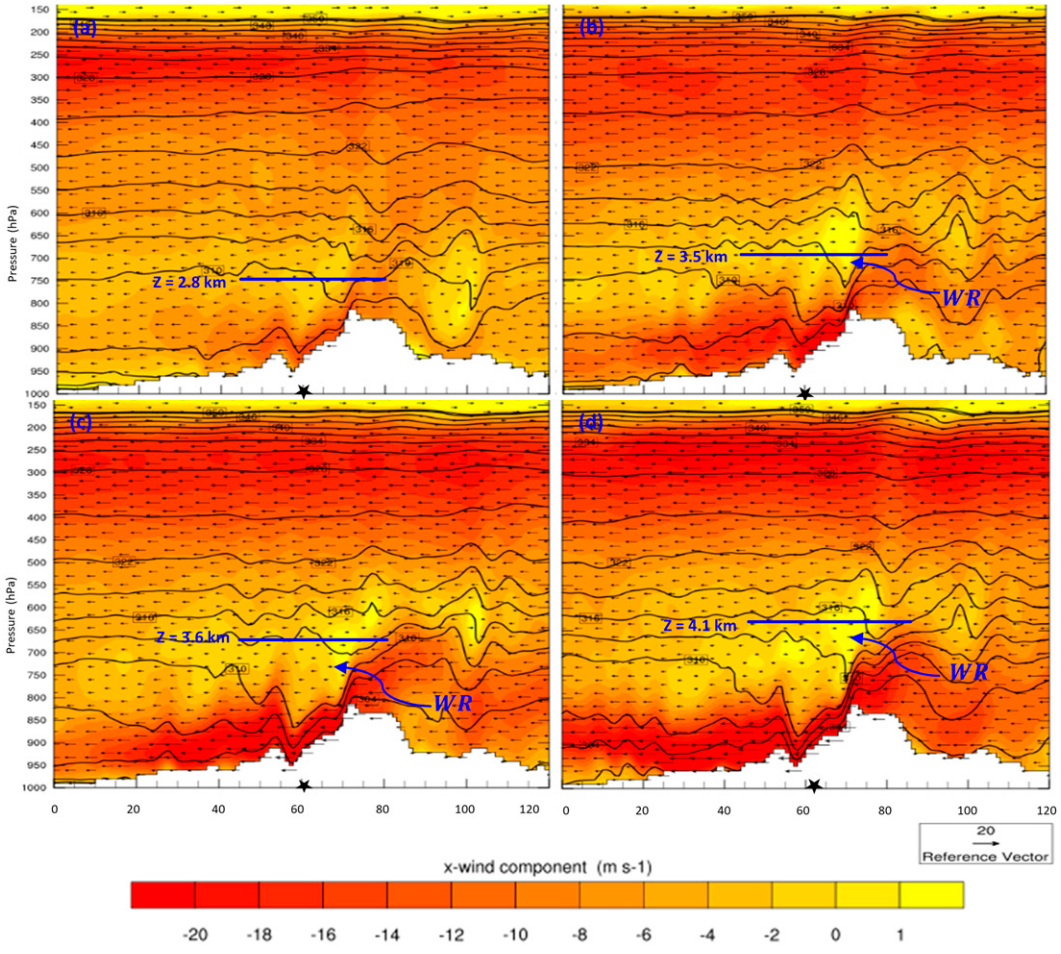

FIG. 13. Cross-sectional analysis of U wind (shaded; m s^{-1}), potential temperature (contours; K), and wind vectors (arrows) valid at (a) 0200 UTC 26 Oct, (b) 0400 UTC 26 Oct, (c) 0600 UTC 26 Oct, and (d) 0800 UTC 26 Oct for D3 (1-km resolution). The blue horizontal lines represent the critical-level heights. Critical-level height is measured by the $Z_c/\lambda_z = 3/4 + n$ formula. The wind reversal level is denoted as WR. The black star depicts the Cedar Fire location.

layer is induced over the peak of the CM, which results from the resonant amplification mechanism, in triggering a severe downslope wind over the lee slope of the CM, and then 3) the further enhancement of this severe downslope wind occurs through the HJ mechanism, which propagates downstream to the Coast Mountain Range.

1) RESONANT AMPLIFICATION MECHANISM

To verify the resonant amplification mechanism, we plan to make an analysis on one cross section over the San Diego coastal region from 32.8°N, 117.26°W to 33.02°N, 116.3°W (see the thick blue line in Fig. 3c) from the D3 domain. Figure 13 shows the cross-sectional analysis of the u wind component, potential temperature, and wind vector valid for 0200 UTC to 0800 UTC 26 October every 2 h. The mountain wave deepens and starts to overturn and/or break above the lee slope while upper-level northeasterly winds exist over the CM (Fig. 13b). The wave-breaking region is identified with the wind reversal (WR) above it (Figs. 13b–d). According to the resonant amplification theory proposed by CP84, wave overturning occurs at the lowest self-induced critical-level height Z_c of $Z_c/\lambda_z = 3/4 + n$, where $n = 0$, 1, 2, …, and $\lambda_z = 2\pi U/N$ = a hydrostatic vertical wavelength. This critical-level height acts as a boundary to reflect the upward-propagating wave energy back toward the mountain surface and inducing downward mountain waves through partial resonance [see Lin (2007) for a brief review]. The upward-propagating waves are generated by mesoscale mountains and break above the mountain's peak, whereas the downward-propagating waves are reflected from the critical level.

To verify this critical-level height for our case, we extracted an upstream sounding from the D3 domain at 32.98°N, 116.42°W for nine different times. The soundings were extracted for several parameters, including potential temperature, u wind, height, and so on, from the upslope of the CM. The extracted sounding data is averaged up to 350-hPa level, and then we calculate the critical-level height

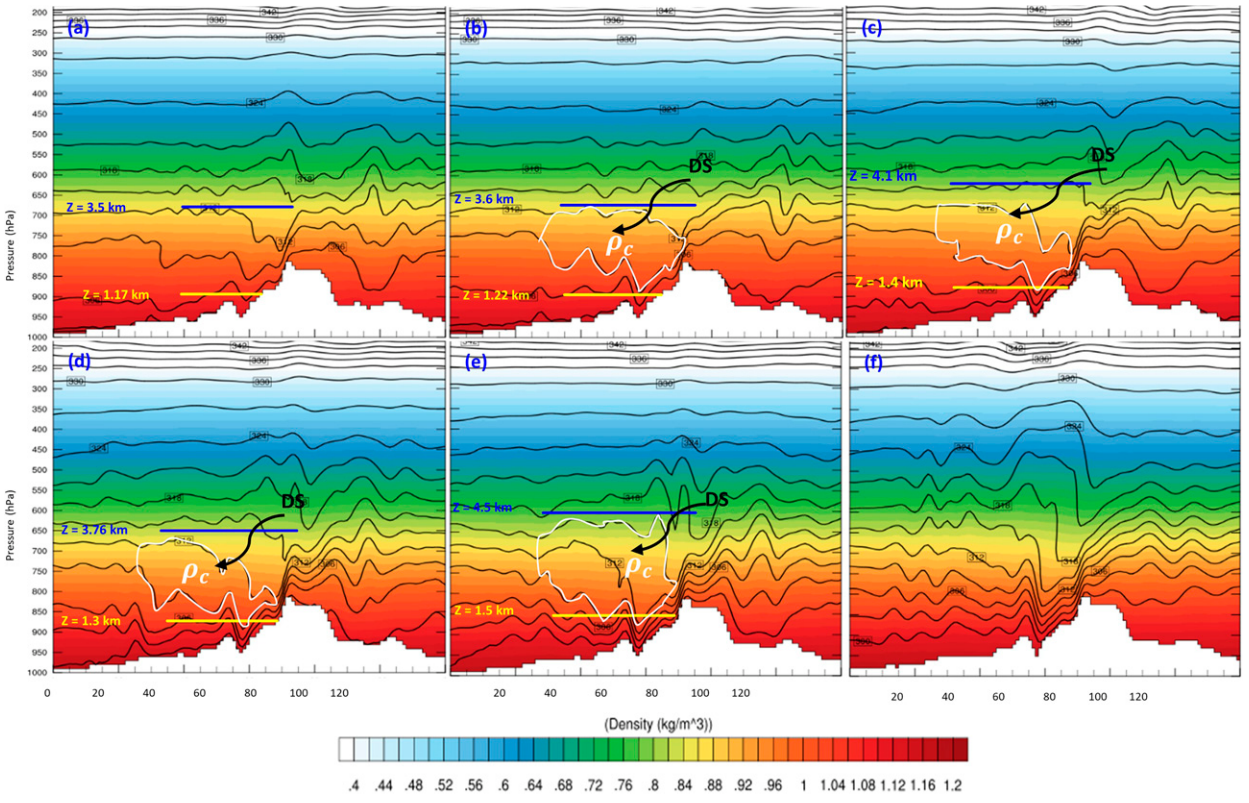

FIG. 14. Cross-sectional analysis of density (shaded; kg m^{-3}) and potential temperature (contours; K) valid at (a) 0400 UTC, (b) 0600 UTC, (c) 0800 UTC, (d) 1000 UTC, (e) 1200 UTC , and (f) 1500 UTC 26 Oct for D3. The uniform density (ρ_c) region is encompassed within the dividing streamline (DS). The blue and yellow horizontal lines represent the critical-level heights calculated using the formula based on CP84 (blue lines) and S85 (blue and yellow lines) theory.

using the formula proposed by CP84 for $n = 0$. Note that at the critical level Z_c the basic wind U coincides with the phase speed of the wave (i.e., at Z_c, $U = C = 0$) and finally reverses its direction. The lowest critical-level height calculated at 0200 UTC 26 October (blue horizontal line in Fig. 13a) is 2.8 km, but it is very early to develop a wind reversal as strong mountain wave breaking is yet to occur. At 0400 UTC 26 October (Fig. 13b), the mountain wave breaking increases above the peak of the CM and the critical-level height is identified at the 3.5-km height level, which coincides with the WR on top of it. This helps to develop static instability with the turbulent mixing starts over the lee slope. Consequently, a severe downslope wind state occurred at the lee slope of the CM through the resonance between the mountain surface and the critical level, at least at this time. However, at later times, for example, 0600 and 0800 UTC 26 October (Figs. 13c,d), the critical-level height (Z_c = 3.6 and 4.1 km) does not coincide with the WR level. At these times, the WR level is identified below the critical-level height. Therefore, it can be concluded that the resonant amplification theory applies at the earlier stage of the development of the severe downslope wind. The later stage of the development of the severe downslope wind will be explained using the HJ mechanism (S85) in the following section.

2) HYDRAULIC JUMP MECHANISM

According to Smith's hydraulic theory (S85), the severe downslope winds form by the interaction between a smoothly stratified flow and the deep, well-mixed region above the lee slope of the mountain (reviewed in Lin 2007). In contrast to resonant amplification theory (CP84), S85's hydraulic theory predicts that the critical-level height is falling within the range of $Z_i/\lambda_z = 1/4 + n$ to $3/4 + n$ during the high-drag or severe-wind state. From our 1-km simulated results, the critical-level height is located within the layer from 1.17 to 3.5 km at 0400 UTC 26 October (yellow and blue horizontal lines in Fig. 14a); from 1.22 to 3.6 km at 0600 UTC 26 October (Fig. 14b); from 1.4 to 4.1 km at 0800 UTC 26 October (Fig. 14c); from 1.3 to 3.8 km at 1000 UTC 26 October (Fig. 14d); and from 1.5 to 4.5 km at 1200 UTC 26 October (Fig. 14e). When a severe-wind state develops above the lee slope of the mountain, a dividing streamline (DS) encompasses a region of uniform density. This uniform density region is identified in our fine-resolution simulation. Figure 14 shows the cross-sectional analysis of the density, potential temperature, along with critical-level height ranges valid from 0400 to 1400 UTC 26 October, with every 2 h. It has been seen that the theta surface splits or divides over the CM at 0600, 0800, 1000, and 1200 UTC 26 October (white outline region in Figs. 14b–e). These splitting theta surfaces are termed DS. The lower

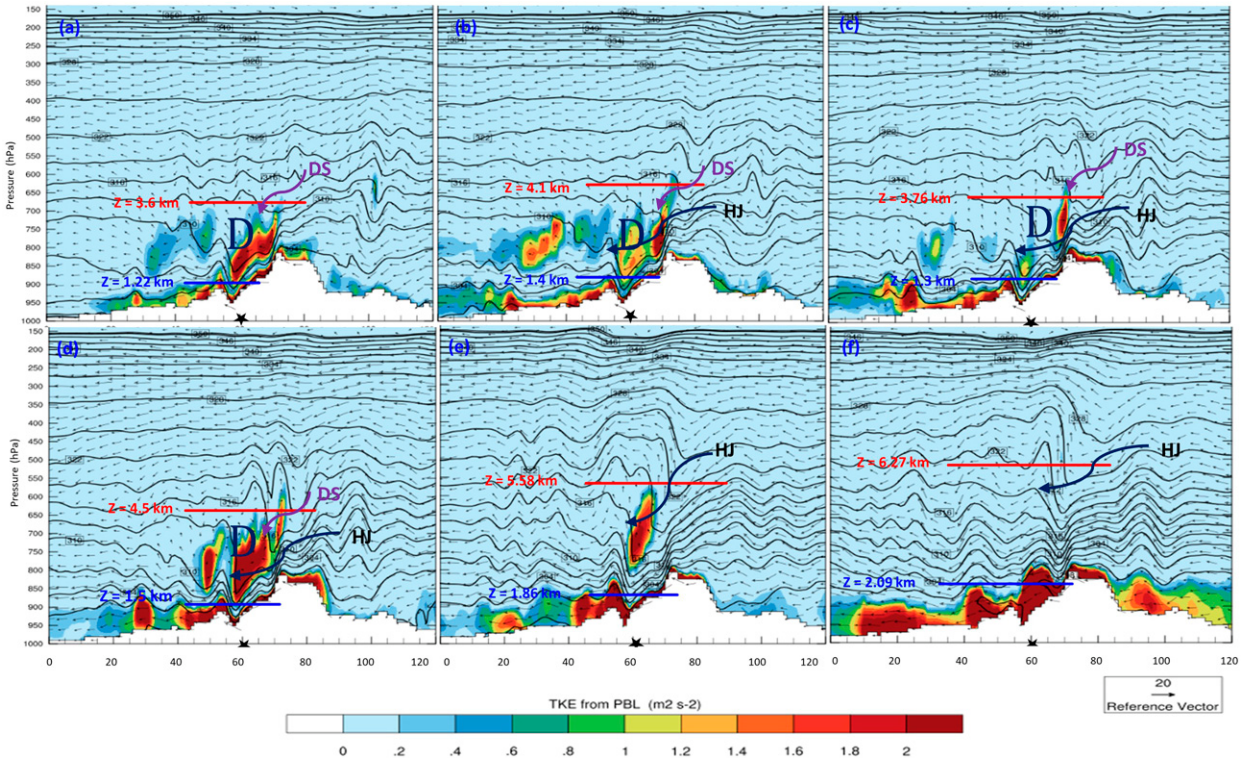

FIG. 15. Cross-sectional analysis of potential temperature (contours; K), turbulent kinetic energy (shaded; $m^2\ s^{-2}$), and wind vectors (arrows) from the 1-km simulation valid at (a) 0600 UTC, (b) 0800 UTC, (c) 1000 UTC, (d) 1200 UTC, (e) 1500 UTC, and (f) 1800 UTC 26 Oct 2003. The red and blue horizontal lines represent the critical-level heights calculated using CP84 (red) and S85 (blue) theory. The dead (D) region is encompassed within a DS. The hydraulic jump is indicated by HJ.

branch of the DS descends rapidly over the lee slope of the CM to the surface. This DS is designated by potential temperature equal to θ_c or within the well-mixed region of uniform density ($\sim\rho_c$) (see the region encompassed by the white outline in Figs. 14b–e). According to the S85's theory, this uniform density region is the well-mixed, turbulent dead (D) region, which is characterized by strong turbulent kinetic energy (TKE), illustrated in Fig. 15. The TKE calculated here is from the boundary layer parameterization, which is subgrid-scale TKE. Figure 15 shows the cross-sectional analysis of potential temperature and TKE with the indication of DS, the D region, and the critical-level heights (red and blue horizontal lines). A strong TKE (maxima ~2 $m^2\ s^{-2}$) region is identified within a DS at 0600 UTC 26 October (Fig. 15a). Afterward, the well-mixed layer deepens as a result of the development of K-H instability in the local region of enhanced shear associated with flow perturbations. The evidence of this deepening region can be seen by increasing the TKE at 0800 UTC 26 October, while a HJ also forms over the lee slope of the CM (Fig. 15b). The wave-breaking region is seen to expand upward and develop some weak and strong HJ with time (Figs. 15c–e). After the HJ formation, the turbulent mixed region expands downward and accelerates downstream by the nonlinear advection (Klemp and Lilly 1975; Lin and Wang 1996) (Figs. 15d–f). Thus, it causes severe downslope winds over the lee slope of the CM, which expanded toward the coastal region of San Diego. How severe this downslope wind is will be examined in the following paragraph.

Figure 16 shows the cross-sectional analysis of total wind speed $(u^2 + w^2)^{1/2}$, potential temperature, and wind vector (u, w) valid from 0400 to 1800 UTC 26 October. The northeasterly wind speed over the lee slope of the CM of ~20 m s^{-1} is observed at 0400 UTC 26 October (Fig. 16a). This leeside wind speed increases with time. At 1200 UTC 26 October (Fig. 16c), the northeasterly upstream winds increase more than 30 m s^{-1}. There was an early dry tongue near the surface of the Southern California coastal region with relative humidity around or less than 15% (not shown) before the extremely dry surge (relative humidity ~5%) descending from the upper-level jet. This extremely dry upper-level air is over the CM along with the strong upstream northeasterly wind. It enhanced the severe downslope wind through the resonant amplification and the HJ mechanisms. At the severe downslope wind stage, strong winds greater than 34 m s^{-1} exist over the lee slope of the CM (Fig. 16d), which transport hot and dry air toward the coastal area of San Diego (Figs. 16e,f).

c. *Impacts of deep-layer resonance on severe downslope winds—An idealized study*

Based on the findings from the terrain sensitivity experiments in section 4a, we propose that the severe downslope

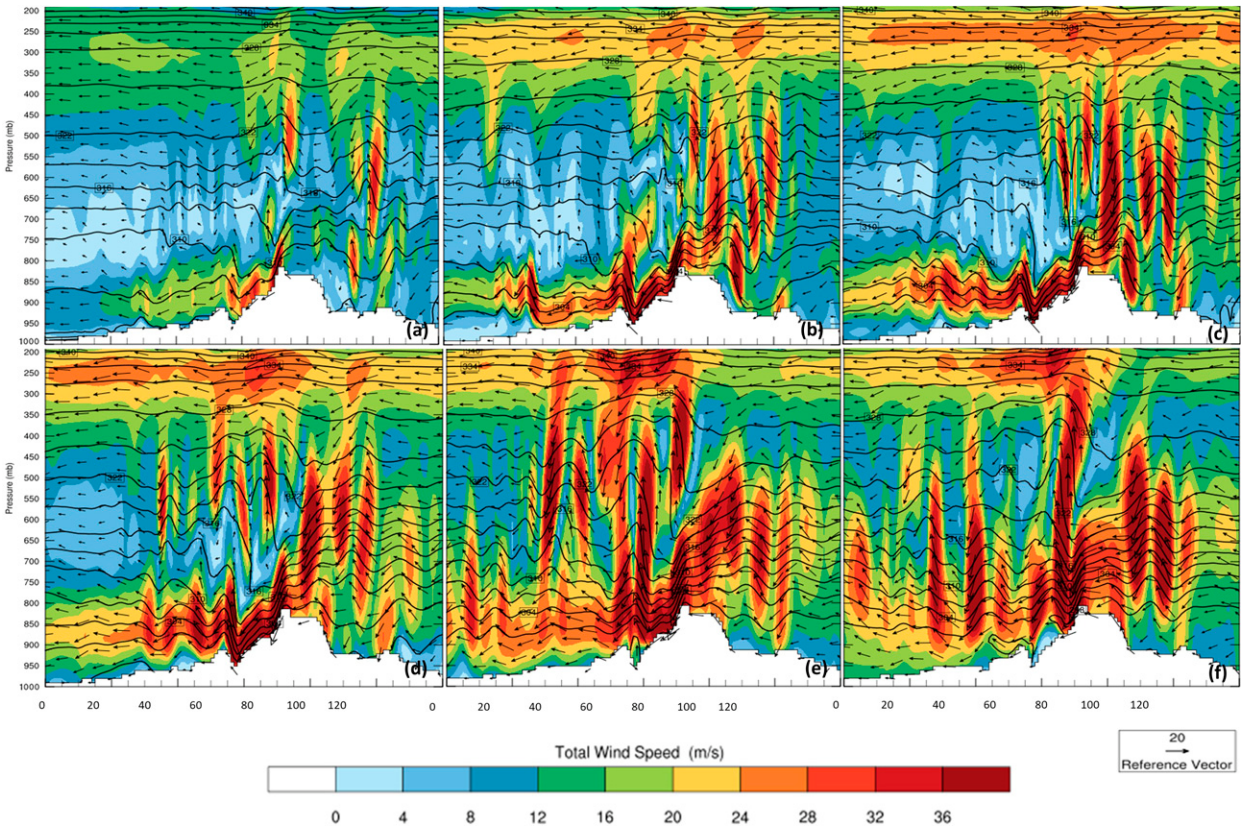

FIG. 16. Cross-sectional analysis of potential temperature (contours; K), total wind speed $(u^2 + w^2)^{1/2}$ (shaded; m s^{-1}), and wind vectors (arrows) from the 1-km simulation valid at (a) 0400 UTC, (b) 1000 UTC, (c) 1200 UTC, (d) 1400 UTC, (e) 1600 UTC, and (f) 1800 UTC 26 Oct 2003.

winds over the lee slope of the CM are produced by nonlinear mountain waves with tropospheric resonance. The basic dynamics of this nonlinear deep-layer resonance mechanism is examined by performing numerical simulations with idealized upstream soundings.

The idealized upstream sounding is composed of several flow and orographic parameters, such as potential temperature, horizontal basic wind U normal to the mountain range, and deep-layer (troposphere) height as extracted from the NoSR simulation at 36.7°N, 108.9°W for three idealized cases, which can be briefly described as (i) ICTL: idealized control case with constant U and two-layer atmosphere with constant Brunt–Väisälä frequency N in each layer, (ii) IJET: same as ICTL except with a jet near the tropopause, and (iii) INN: same as ICTL except with no vertical variation of the N (i.e., no stratosphere with constant $N = 0.01$ s^{-1}). Case ICTL has a uniform wind speed of -7.5 m s^{-1} from the surface to the domain top (Fig. 17c). The idealized potential temperature θ profile is obtained by performing a vertical integration with respect to z using the formula, $N^2 = (g/\theta_0)(\partial\theta/\partial Z)$ (Fig. 17a), where g is the gravitational acceleration, assuming a Boussinesq atmosphere. The structured N used in this case is 0.01 s^{-1} from the surface to 11 km and 0.02 s^{-1} from 11 km to the model top (Fig. 17b). The IJET case is identical to the ICTL, except there exists an upper-level jet with a jet wind core of 30 m s^{-1}. In this case, the basic wind speed U is set as $U_0 = -7.5$ m s^{-1} from $z = 0$ to 8 km and from $z = 14$ km to model top. From $z = 8$ to 14 km, U increases up to 30 m s^{-1} by using the formula

$$U(z) = U_0 + (U_J - U_0)\cos\left[\frac{\pi}{Z_H}(z - z_J)\right],$$

where $U_J = -30$ m s^{-1} is jet core speed, $U_0 = -7.5$ m s^{-1}, $Z_H = 6$ km is the depth of jet, and $Z_J = 11$ km is the height of the jet core (Fig. 18a). Case IJET will allow us to understand how much impact the jet has on the mountain waves. To specifically diagnose the impact of the reflection of the stratosphere on producing the downslope winds, the INN case is run by keeping N constant (=0.01 s^{-1}) all the way to the model top (Fig. 18b).

The case NoSR-simulated results are compared with all three idealized cases to help to understand the basic generation mechanisms of the severe downslope winds over the lee slope of the CM. Figure 19 shows the vertical velocities and the isentropes for both real and idealized cases, which is used to examine whether there is a resonance between the mountain surface and the tropopause. In the NoSR case (Fig. 19a), the upward-energy-propagating mountain waves (i.e., the wave energy is able to propagate vertically) are

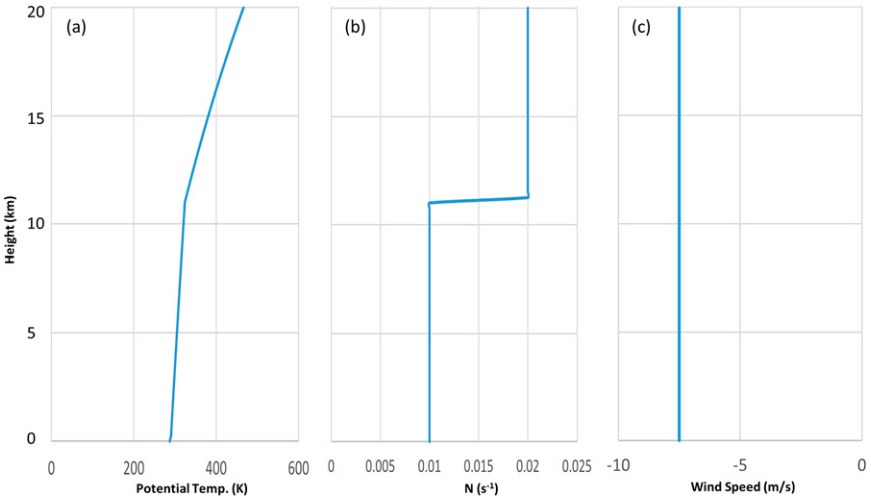

FIG. 17. Vertical profiles of idealized (a) potential temperature θ, (b) Brunt–Väisälä frequency N, and (c) uniform wind speed U for the ICTL experiment.

identified with an upstream phase tilt (toward the right with height) over the peak of the CM, based on Eliassen and Palm's theorem [see, e.g., discussion on p. 113 of Lin (2007)]. On the other hand, when the airflow is passing over the CM, the phase is oriented vertically, indicating a possible resonance between the mountain surface and the tropopause. The ICTL case (Fig. 19b), which uses a mountain height of 1.5 km and uniform basic wind with a structured N profile (Fig. 17b), exhibits a shallow layer of trapped waves located between $z = 4$ and 7 km. These trapped waves resulted from the resonance between the mountain surface and the tropopause, not between the mountain surface and the critical-level height, as proposed by CP84. The resonance in the ICTL case is produced by both the orographically induced gravity waves (i.e., mountain waves) and the sudden increase of N at the tropopause. The sensitivity of N to resonance can be differentiated by using a uniform N ($=0.01\ s^{-1}$; case INN) instead of the structured N used in the ICTL case. When N is constant throughout the lower (troposphere) and the upper layer (stratosphere), we no longer see strong reflection (Fig. 19d) in comparison with that in case ICTL (Fig. 19b). Since N is weaker ($0.01\ s^{-1}$) in case INN than in case ICTL ($0.02\ s^{-1}$) in the upper layer, more wave energy can propagate to the upper layer. In the case ICTL, significantly more wave energy is reflected back to the troposphere. We see strong vertically propagating gravity waves in the IJET case (Fig. 19c), but there is no resonance in the midtroposphere.

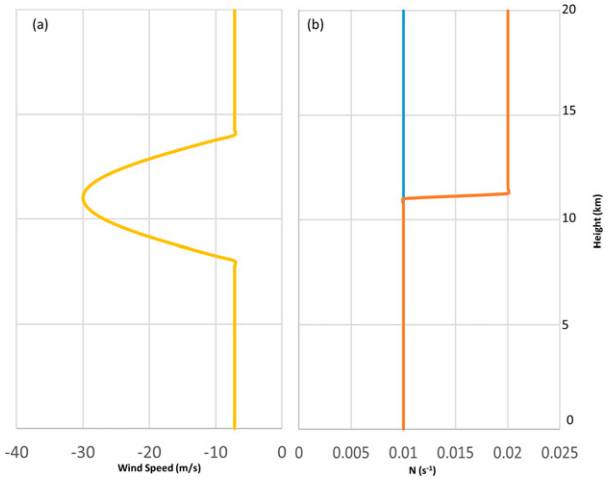

FIG. 18. Vertical profiles of idealized jet wind speed for the (a) IJET case, which is identical to the ICTL case except with the upper-level jet, and (b) INN case, which is identical to the ICTL case except that the N is kept constant.

Because of the resonance between the mountain surface and the tropopause, part of the energy is reflected back to the lower levels, which leads to wave steepening, overturning, and turbulence over the lee slope of the mountain. The total wind analysis, as shown in Fig. 20, helps to identify this region of turbulence over the lee slope. The presence of severe downslope winds over the lee slope of the mountain can be identified in all cases including, real NoSR (Fig. 20a), idealized ICTL (Fig. 20b), IJET (Fig. 20c), and INN (Fig. 20d). The well-developed HJ in the lower levels is also present for all idealized cases, which helps to produce strong winds near the mountain surface farther downstream.

Case NoSR's downstream wave propagation is seen more clearly from the fine-resolution (i.e., D3, 1 km) simulated results (see Fig. 16). The severe downslope wind in the ICTL case is produced due to resonance from larger N and the uniform lower-level basic wind. There is no strong evidence that the jet streak plays a significant role in helping the development of the severe downslope wind in comparison with the deep-layer resonance. It, however, does change the structure in the tropopause. On the other hand, the severe downslope wind in the IJET case is produced by the lower-layer wind (Fig. 20c).

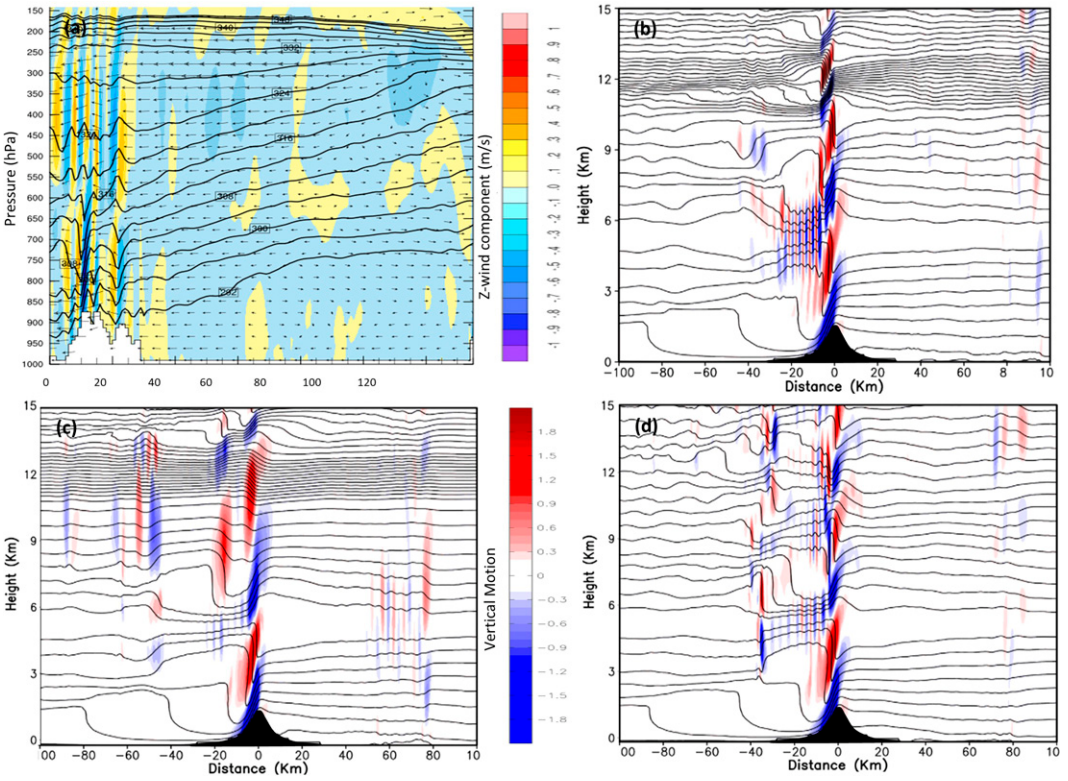

FIG. 19. Vertical velocities (shaded; m s^{-1}), and isentropes (contours) for (a) the real NoSR case valid at 0800 UTC 26 Oct 2003 and idealized cases (b) ICTL, (c) IJET, and (d) INN after 12-h simulations.

Unlike case ICTL, in the INN case, there is a strong jet at height level $z = 4.7$ km (Fig. 20d), which can be explained by the second HJ that develops at approximately $z = 7$ km. This second HJ is more well-developed in the horizontal than that in the case of ICTL due to the trapping of the air between the strong second HJ and that over the mountain surface. Therefore, based on our findings, Lin (2007) may be modified to "both the resonance mechanism and HJ mechanism are persistent and prevail all the time except the HJ is more well developed at the later stage."

In summary, by comparing idealized ICTL, IJET, and INN cases, a larger-scale jet is not necessary to produce severe downslope wind over the lee slope of the mountain. The downslope wind in the ICTL case responds to the resonance between the mountain surface and the tropopause, which comes mainly from the more stable layer. However, such a jet may be instrumental in establishing a favorable vertical stratification for severe downslope winds.

5. Conclusions

This study investigates the formation mechanism of the mesoscale environments conducive to the severe downslope wind during the Cedar Fire on 25–29 October 2003 by conducting numerical simulations using the WRF-ARW model. In particular, we studied the impact of the interaction between upper- and lower-level flows and also the influence of the southern portion of the SaR extending to MR, and the SoR on the mesoscale environment over the lee slope of the CM near San Diego. We hypothesize that there exist three consecutive stages experienced by the flow in forming the mesoscale environment conducive to the downslope windstorm: (i) the easterly jet in the upper-troposphere is forced downward by the sinking motion associated with a jet streak upstream of the sequence of mountain ranges, (ii) a critical layer is induced over the peak of the CM, which results from the resonant amplification mechanism, in triggering a severe downslope wind over the lee slope of the CM, and then (iii) the further enhancement of this severe downslope wind occurs through the HJ mechanism, which propagates downstream to the Coast Mountain Range.

Four real data sensitivity cases were conducted, including the CNTL case with one-way triple nested domains starting from16 km down to 1 km and three terrain sensitivity experiments run on a 16-km grid by removing specific mountain ranges such as removing SaR (NoSa), removing SoR (NoRo), and removing both SaR and SoR (NoSR). In addition, three idealized simulations, including idealized control (ICTL) (with uniform basic wind and structured Brunt–Väisälä frequency N), IJET (with strong upper-level jet), INN (with constant $N = 0.01$ s^{-1}) have also been conducted to understand the mechanisms for producing severe downslope winds by nonlinear mountain waves while air flows over the mountain.

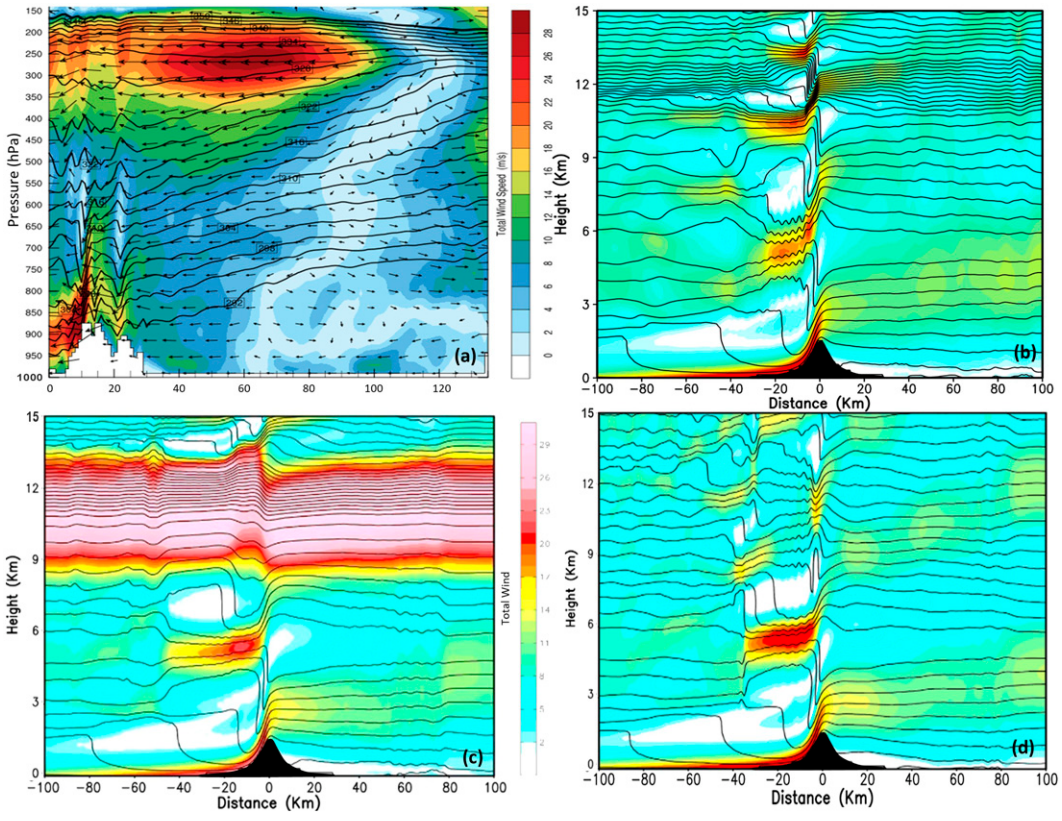

FIG. 20. Total wind speed $(u^2 + w^2)^{1/2}$ (shaded; m s^{-1}) and isentropes (contours) for (a) the real NoSR case valid at 0800 UTC 26 Oct 2003 and idealized cases (b) ICTL, (c) IJET, and (d) INN after 12-h simulations.

For the upper-level forcing mechanism, the downward motion in the jet exit region penetrates to the top of the PBL, descending directly over the southern portion of the SaR and SoR in southwestern Colorado. By comparing cases CNTL, NoSa, NoRo, and NoSR, it is evident that the SaR and the SoR do not play significant roles in producing the severe downslope wind over the CM. In fact, these two mountain ranges have modified the upstream condition, which negatively impacts the severe downslope wind. Hence, it is concluded that the sinking motion associated with the upper-level jet streak appears to be able to enhance the downslope winds over the CM without being essential to their formation.

While upper-level forcing is coupled with the lower-layer orographic forcing, the resonant amplification mechanism takes place as mountain waves amplify and break. Once wave breaking happens, the critical level is induced with a wind reversal on top of it. The wave-breaking region acts as an internal boundary that reflects the upward-propagating waves back to the ground and produces a high drag state associated with a HJ. When a high drag or severe wind state develops above the lee slope of the mountain, a DS encompasses a uniform density region characterized by well-mixed turbulence. The strong turbulent mixing region starts to expand downward because of K-H instability, which helps to produce severe downslope winds following the HJ toward the San Diego coastal region.

The basic dynamics of severe downslope winds produced by nonlinear mountain waves with troposphere resonance are studied using idealized numerical simulations with upstream soundings and idealized mountains. By comparing real NoSR, and idealized ICTL, IJET, and INN cases, it is found that the larger-scale jet does not play a significant role in producing severe downslope wind over the lee slope of the mountain. The downslope wind in the ICTL case responds to the deep-layer resonance between the mountain surface and the tropopause, which comes mainly from both the orographically induced gravity waves (i.e., mountain waves) and the sudden increase of N at the tropopause. Case ICTL exhibits a shallow layer of trapped waves located between $z = 4$ and 7 km. These trapped waves resulted from the resonance between the mountain surface and the tropopause, not between the mountain surface and the critical-level height, as proposed by CP84.

In summary, the jet streak's downward motion is complementary to but not necessary to produce severe downslope winds in this case study of the environment facilitating the Cedar Fire. The downslope wind over the lee slope of the CM is produced mainly by the deep-layer resonance between the mountain surface and the tropopause.

Acknowledgments. This research is supported by the National Science Foundation Awards 1900621 and 2022961. The authors acknowledge the Computational and Information

Systems Laboratory (CISL) for their support of computing time on the Cheyenne supercomputer (Project UNCS0030 and UNCT0001).

Data availability statement. The GFS data using this study are openly available from the NCAR's Research Data Archive (https://doi.org/10.5065/D6M043C6) as cited in NCEP (2000). The ERA5 data using this study are openly available from the NCAR's Research Data Archive (https://doi.org/10.5065/BH6N-5N20) as cited in ECMWF (2019).

REFERENCES

CAL FIRE, 2003: Cedar Fire incident information. The California Department of Forestry and Fire Protection, https://www.fire.ca.gov/incidents/2003/10/25/cedar-fire/.

——, 2021: Top 20 largest California wildfires. The California Department of Forestry and Fire Protection, https://www.fire.ca.gov/media/4jandlhh/top20_acres.pdf.

Cao, Y., and R. G. Fovell, 2016: Downslope windstorms of San Diego County. Part I: A case study. *Mon. Wea. Rev.*, **144**, 529–552, https://doi.org/10.1175/MWR-D-15-0147.1.

Clark, A. J., C. J. Schaffer, W. A. Gallus, and K. Johnson-O'Mara, 2009: Climatology of storm reports relative to upper-level jet streaks. *Wea. Forecasting*, **24**, 1032–1051, https://doi.org/10.1175/2009WAF2222216.1.

Clark, T. L., and W. R. Peltier, 1977: On the evolution and stability of finite-amplitude mountain waves. *J. Atmos. Sci.*, **34**, 1715–1730, https://doi.org/10.1175/1520-0469(1977)034<1715:OTEASO>2.0.CO;2.

——, and ——, 1984: Critical level reflection and the resonant growth of nonlinear mountain waves. *J. Atmos. Sci.*, **41**, 3122–3134, https://doi.org/10.1175/1520-0469(1984)041<3122:CLRATR>2.0.CO;2.

Doyle, J. D., M. A. Shapiro, Q. Jiang, and D. L. Bartels, 2005: Large-amplitude mountain wave breaking over Greenland. *J. Atmos. Sci.*, **62**, 3106–3126, https://doi.org/10.1175/JAS3528.1.

——, and Coauthors, 2011: An intercomparison of T-REX mountain-wave simulations and implications for mesoscale predictability. *Mon. Wea. Rev.*, **139**, 2811–2831, https://doi.org/10.1175/MWR-D-10-05042.1.

Durran, D. R., 1990: Mountain waves and downslope winds. *Atmospheric Processes over Complex Terrain*, R. M. Banta et al., Eds., Vol. 23, Amer. Meteor. Soc., 59–81, https://doi.org/10.1007/978-1-935704-25-6_4.

——, and J. B. Klemp, 1987: Another look at downslope winds. Part II: Nonlinear amplification beneath wave-overturning layers. *J. Atmos. Sci.*, **44**, 3402–3412, https://doi.org/10.1175/1520-0469(1987)044<3402:ALADWP>2.0.CO;2.

ECMWF, 2019: ERA5 reanalysis (0.25° latitude-longitude grid). National Center for Atmospheric Research Computational and Information Systems Laboratory Research Data Archive, accessed 29 January 2022, https://doi.org/10.5065/BH6N-5N20.

Glickman, T. S., 2000: *Glossary of Meteorology*. 2nd ed. Amer. Meteor. Soc., 855 pp.

Huang, C., Y. L. Lin, M. L. Kaplan, and J. J. Charney, 2009: Synoptic-scale and mesoscale environments conducive to forest fires during the October 2003 extreme fire event in Southern California. *J. Appl. Meteor. Climatol.*, **48**, 553–579, https://doi.org/10.1175/2008JAMC1818.1.

Iacono, M. J., J. S. Delamere, E. J. Mlawer, M. W. Shephard, S. A. Clough, and W. D. Collins, 2008: Radiative forcing by long-lived greenhouse gases: Calculations with the AER radiative transfer models. *J. Geophys. Res.*, **113**, D13103, https://doi.org/10.1029/2008JD009944.

Jang, W., and H.-Y. Chun, 2010: A numerical study on severe downslope windstorms occurred on 5 April 2005 at Gangneung and Yangyang, Korea. *Asia-Pac. J. Atmos. Sci.*, **46**, 155–172, https://doi.org/10.1007/S13143-010-0015-2.

Janjić, Z. I., 1994: The step-mountain eta coordinate model: Further developments of the convection, viscous sublayer, and turbulence closure schemes. *Mon. Wea. Rev.*, **122**, 927–945, https://doi.org/10.1175/1520-0493(1994)122<0927:TSMECM>2.0.CO;2.

Johnson, D. L., 2004: Southern California wildfires October 20 to November 3, 2003. NOAA/NWS Service Assessment Doc., 45 pp., https://repository.library.noaa.gov/view/noaa/6470.

Kain, J. S., 2004: The Kain–Fritsch convective parameterization: An update. *J. Appl. Meteor. Climatol.*, **43**, 170–181, https://doi.org/10.1175/1520-0450(2004)043<0170:TKCPAU>2.0.CO;2.

Karim, S. M. S., and Y.-L. Lin, 2021: A study of track deflection associated with the landfall of Tropical Cyclone Sidr (2007) over the Bay of Bengal and Bangladesh. *Dyn. Atmos.–Ocean*, **93**, 101207, https://doi.org/10.1016/j.dynatmoce.2021.101207.

Klemp, J. B., and D. R. Lilly, 1975: The dynamics of wave-induced downslope winds. *J. Atmos. Sci.*, **32**, 320–339, https://doi.org/10.1175/1520-0469(1975)032<0320:TDOWID>2.0.CO;2.

Lin, Y.-L., 2007: *Mesoscale Dynamics*. Cambridge University Press, 630 pp.

——, and T.-A. Wang, 1996: Flow regimes and transient dynamics of two-dimensional stratified flow over an isolated mountain ridge. *J. Atmos. Sci.*, **53**, 139–158, https://doi.org/10.1175/1520-0469(1996)053<0139:FRATDO>2.0.CO;2.

——, R. D. Fairly, and H. D. Orville, 1983: Bulk parameterization of the snowfield in a cloud model. *J. Appl. Meteor. Climatol.*, **22**, 1065–1092, https://doi.org/10.1175/1520-0450(1983)022<1065:BPOTSF>2.0.CO;2.

Long, R. R., 1953: Some aspects of the flow of stratified fluids: Part I. A theoretical investigation. *Tellus*, **5**, 42–58, https://doi.org/10.3402/tellusa.v5i1.8563.

Lott, F., 2016: A new theory for downslope windstorms and trapped mountain waves. *J. Atmos. Sci.*, **73**, 3585–3597, https://doi.org/10.1175/JAS-D-15-0342.1.

Mlawer, E. J., S. J. Taubman, P. D. Brown, M. J. Iacono, and S. A. Clough, 1997: Radiative transfer for inhomogeneous atmospheres: RRTM, a validated correlated-*k* model for the longwave. *J. Geophys. Res.*, **102**, 16 663–16 682, https://doi.org/10.1029/97JD00237.

Monin, A. S., and A. M. Obukhov, 1954: Basic laws of turbulent mixing in the surface layer of the atmosphere. *Tr. Geofiz. Inst., Akad. Nauk SSSR*, **24**, 163–187.

NCEP, 2000: NCEP FNL operational model global tropospheric analyses, continuing from July 1999. Research Data Archive at the National Center for Atmospheric Research, Computational and Information Systems Laboratory, accessed 17 November 2019, https://doi.org/10.5065/D6M043C6.

Peltier, W. R., and T. L. Clark, 1979: The evolution and stability of finite-amplitude mountain waves. Part II: Surface wave drag and severe downslope windstorms. *J. Atmos. Sci.*, **36**, 1498–1529, https://doi.org/10.1175/1520-0469(1979)036<1498:TEASOF>2.0.CO;2.

Rolinski, T., S. B. Capps, and W. Zhuang, 2019: Santa Ana winds: A descriptive climatology. *Wea. Forecasting*, **34**, 257–275, https://doi.org/10.1175/WAF-D-18-0160.1.

Scinocca, J. F., and W. R. Peltier, 1993: The instability of long's stationary solution and the evolution toward severe downslope windstorm flow. Part I: Nested grid numerical simulations. *J. Atmos. Sci.*, **50**, 2245–2263, https://doi.org/10.1175/1520-0469(1993)050<2245:TIOLSS>2.0.CO;2.

Skamarock, W. C., and Coauthors, 2019: A description of the Advanced Research WRF Model version 4. NCAR Tech. Note NCAR/TN-556+STR, 145 pp., https://doi.org/10.5065/1dfh-6P97.

Small, I. J., 1995: Santa Ana winds and the fire outbreak of fall 1993. NOAA Tech. Memo. NWS WR-230, 56 pp., https://repository.library.noaa.gov/view/noaa/14448.

Smith, R. B., 1979: The influence of mountains on the atmosphere. *Adv. Geophys.*, **21**, 87–230, https://doi.org/10.1016/S0065-2687(08)60262-9.

——, 1985: On severe downslope winds. *J. Atmos. Sci.*, **42**, 2597–2603, https://doi.org/10.1175/1520-0469(1985)042<2597:OSDW>2.0.CO;2.

Sommers, W. T., 1978: LFM forecast variables related to Santa Ana wind occurrences. *Mon. Wea. Rev.*, **106**, 1307–1316, https://doi.org/10.1175/1520-0493(1978)106<1307:LFVRTS>2.0.CO;2.

Stein, A. F., R. R. Draxler, G. D. Rolph, B. J. B. Stunder, M. D. Cohen, and F. Ngan, 2015: NOAA's HYSPLIT atmospheric transport and dispersion modeling system. *Bull. Amer. Meteor. Soc.*, **96**, 2059–2077, https://doi.org/10.1175/BAMS-D-14-00110.1.

Sun, W.-Y., and S.-H. Chen, 2002: A one-dimensional time-dependent cloud model. *J. Meteor. Soc. Japan*, **80**, 99–118, https://doi.org/10.2151/jmsj.80.99.

Tewari, M., and Coauthors, 2004: Implementation and verification of the unified Noah land-surface model in the WRF model. *20th Conf. on Weather Analysis and Forecasting/16th Conf. on Numerical Weather Prediction*, Seattle, WA, Amer. Meteor. Soc., 14.2a, https://ams.confex.com/ams/pdfpapers/69061.pdf.

Wang, T.-A., and Y.-L. Lin, 1999: Wave ducting in a stratified shear flow over a two-dimensional mountain. Part II: Implications for the development of high-drag states for severe downslope windstorms. *J. Atmos. Sci.*, **56**, 437–452, https://doi.org/10.1175/1520-0469(1999)056<0437:WDIASS>2.0.CO;2.